phys. stat. sol. (b) **181**, 133 (1994)

Subject classification: 71.36 and 71.45; 71.25; 73.40; S7.15

Fachbereich Physik der Martin-Luther-Universität Halle[1])

Effect of the Image Potential on Plasmons in Cylindrical Quantum-Well Wires

By

L. WENDLER and V. G. GRIGORYAN

The collective electronic excitations in quasi-one-dimensional cylindrical quantum-well wires are studied theoretically. Using a two-subband model the dispersion curves of the intra- and intersubband plasmons in the random-phase approximation for the cases of one and two occupied subbands are calculated. The influence of the image forces on the intra- and intersubband plasmon is studied in detail. New explicit analytical expressions for the dispersion relations, valid in a wide range of the wave vector are derived. It is shown that the additional intrasubband plasmon, arising if two subbands are occupied, has for small wave vectors a linear dispersion and is independent of the dielectric screening of the quantum-well wire. The intersubband plasmon is split in two branches, one with a positive and one with a negative dispersion. The electric dipole moment of the collective excitations is calculated and the selection rules for the coupling of light with the plasmons are derived.

1. Introduction

The development of molecular-beam epitaxy as a technique for the growth of in atomic-scale precise layered semiconductors has given a new dimension to the study of the properties of narrow-channel semiconductor microstructures. Advances in high-resolution submicrometer lithography and etching techniques make it possible to fabricate *semiconductor nanostructures* in which the electron motion is confined in two or three spatial directions. The study of these low-dimensional or *quantum-confined* systems has gained a great deal of attention in the past few years. GaAs and InSb are the first semiconductors in which the artificial realization of electron systems in all four dimensions, from three dimensions (3D) to quasi-zero-dimension (Q0D), is possible.

In *quasi-two-dimensional* (Q2D) systems, i.e. *heterojunctions* and *quantum wells* (QW), the electron motion is quasi-free parallel to the heterointerfaces, but quantum-confined within a very narrow channel perpendicular to the heterointerfaces (growth direction). Hence, Q2D systems are typified by an energy spectrum consisting of quantum-confined levels (size-quantization) in growth direction, the discrete *electric subbands*, with typical energy separation $\Delta\mathscr{E} \approx 20$ to 200 meV, and a free motion dispersion within the perpendicular plane.

Additional lateral confinement leads to Q1D systems, i.e. *quantum-well wires* (QWW) for which the electron motion is only free in one spatial direction, but confined in growth direction of the structure and in the lateral direction. Quantum-confinement in all three spatial directions results in Q0D systems with totally discrete energy spectrum. Quantum-confined energy levels in lateral direction are obtained by imposing an additional potential, acting on a very short scale, on a Q2D system containing a high mobility quasi-two-

[1]) Friedemann-Bach-Platz 6, D-06108 Halle, Federal Republic of Germany.

dimensional electron gas (Q2DEG). In principle two different types of samples should be distinguished: (i) deep-mesa etched structures and (ii) nanostructured field-effect devices. Now it is also possible to fabricate Q1D and Q0D systems directly by molecular-beam epitaxy, using macrosteps on semiconductor surfaces. This method should be capable of growing samples with smaller lateral widths than the lithographic technique.

Besides of the great deal of interest from the technological point of view, these low-dimensional semiconductor nanostructures offer an excellent opportunity to experimentally study some of the new fundamental concepts of condensed matter theory. This is possible because the most important physical parameters of these systems can be changed in a wide range. If for instance the *phase-coherence length* is always larger than the characteristic length of the sample and changing the characteristic length of the sample from larger than the *elastic mean free path* of the electrons to smaller, the transport properties change from the *diffusive regime* with the typical *universal conductance fluctuations* to the *ballistic regime*. In this regime the transport through a nanostructure shows quantized conductance steps [1, 2].

Apart from the very interesting transport properties of low-dimensional semiconductor nanostructures, their collective excitation spectrum is one of the most fundamental properties. This spectrum depends characteristically on the dimensionality of the system. The most prominent collective excitation of *modulation-doped semiconductor nanostructures* is the *plasmon* and if a magnetic field is applied the *magnetoplasmon*. The interest in the experimental study of plasmons arises also from the possibility that with the charge density of the electron gas many related physical properties, e.g. Fermi energy, Fermi wave vector, etc., can be varied. This allows a detailed investigation of different mechanisms that determine the plasmon resonance itself and the interaction of plasmons with different types of collective excitations. Plasmons and magnetoplasmons have been explored experimentally [3 to 11] and theoretically without [12 to 35] and with magnetic field [36 to 40] in isolated QWWs and lateral multiwire superlattices. The theoretical works on Q1D plasmons predict, according to the size-quantization, two different types of excitations, *intrasubband plasmons* which are connected with electron motion within one subband, and *intersubband plasmons* which are connected with electron motion between two different subbands. It was first shown by Chaplik and Krasheninnikov [51] that the intrasubband plasmon shows a logarithmic dispersion $\omega \propto |\boldsymbol{q}|\, a[-\ln(|\boldsymbol{q}|\, a)]^{1/2}$ for small one-dimensional wave vectors $\boldsymbol{q}$. The constant a depends on the wire size and is equal to the width of the rectangular potential [12], to the radius of the cylindrical potential [24], or to the characteristic width of a harmonic potential [25]. It is noticeable that the characteristic size of the wire enters the lowest-order term of an expansion in powers of $\boldsymbol{q}$ of the intrasubband plasmon dispersion in difference to the corresponding plasmon of the Q2DEG (see for instance [41]). Most of the theoretical works were done using the random-phase approximation (RPA) to calculate the linear response to an external charge [12 to 34, 36, 38 to 40]. Mendoza and Schaich [35] investigated the intrasubband plasmons using a hydrodynamic model including the case of many occupied subbands. For the case that more than one subband is occupied Li and Das Sarma [15, 27], Que [28], and Wendler et al. [29 to 32] calculated the intrasubband plasmons using the quantum-mechanical linear response theory in the RPA. In [29] it was shown that the intrasubband plasmons of the higher occupied subbands exist in gaps between the single-particle intrasubband continua and are free of Landau damping. It is noticeable that for a Q2DEG such gaps in the single-particle continua do not exist. Using an approximate sum rule, Que [28] concluded that for a lateral multiwire system with M populated subbands, one should observe experimentally only one intrasubband plasmon mode.

The first quantum theory of intersubband plasmons was presented by Que and Kirczenow [13]. It was shown for the case of a parabolic confinement potential in a lateral multiwire superlattice that one intersubband plasmon with frequency well beyond the subband separation frequency exists and there are other intersubband plasmons with frequencies close to the subband separation frequency. In this paper the authors predict that only that intersubband plasmon with a large depolarization shift creates a large electric dipole moment which should be observable in optical experiments. Intersubband plasmons in QWWs are investigated in detail by Li and Das Sarma [15, 27], Hu and O'Connell [33], and Wendler et al. [29 to 32]. It is shown [16, 27, 29] that the coupling between intra- and intersubband plasmons in QWWs is more pronounced than in case of Q2D systems. Exploring intersubband plasmons in QWWs for the case that more than one subband is occupied, it was shown firstly by Wendler et al. [29] and Mendoza and Schaich [34] that in the additional regions, which are between the single-particle intersubband continua and free of Landau damping, *new additional branches of intersubband plasmons exist.*

Wendler et al. [29 to 32] investigated in detail the *depolarization shift* of intersubband plasmons. The depolarization shift is the energy difference between a collective intersubband transition, the intersubband plasmon, and the corresponding single-particle intersubband transition, caused by resonance screening. For an initial parabolic confinement potential (bare potential) it was shown [32] by self-consistent calculation of the ground state and response properties of a Q1DEG that the lowest intersubband plasmon has for nearly vanishing wave vector a frequency nearly identical with the bare harmonic oscillator frequency, independent of the density of the Q1DEG. This is a result of the generalized Kohn theorem [42]. Hu and O'Connell [25] investigated intersubband plasmons in a QWW with a parabolic confinement potential within the RPA. They show, that if one increases the magnitude of the gate voltage (such as in experiments of Hansen et al. [3] and Brinkop et al. [4]), which would effectively increase the subband separation and decrease the Fermi energy, the largest frequency of the intersubband plasmon modes displays a quantum-oscillation behaviour but with an overall increasing trend.

Firstly, *retardation* effects on intra- and intersubband plasmons in QWWs were investigated by Wendler et al. [43].

The first *far-infrared* (FIR) *transmission experiment* was carried out by Hansen et al. [3] on magnetoplasmons in a Q1D system. In this paper collective intersubband resonances and intersubband magnetoplasmons were investigated propagating in the direction perpendicular to the wire axis in a lateral multiwire superlattice. It was found that the resonance frequency has a large depolarization shift and increases with decreasing density of the Q1DEG. Brinkop et al. [4] and Demel et al. [5] observed in FIR transmission that the collective intersubband resonance has a very large depolarization shift, up to four times larger than the subband separation. The first experiment on plasmons and magnetoplasmons propagating along the wire axis was performed by Demel et al. [7]. In a recent FIR transmission experiment Drexler et al. [8] showed that the principal collective intersubband resonance is split in three modes above and below the frequency $\omega = \sqrt{2}\,\omega_c$ ($\omega_c = eB/m_c$ is the cyclotron frequency) at higher gate bias. Plasmons [9], magnetoplasmons [10], and spin-density waves [11] of the Q1DEG in GaAs–$Ga_{1-x}Al_xAs$ QWWs have been firstly determined in *resonant inelastic light scattering*. It was found [9] that the intrasubband plasmon shows a linear dispersion, and in contrast, intersubband plasmons appear as dispersionless and have a negligible shift from the single-particle energy.

In this paper we give a detailed investigation of plasmons in cylindrical quantum-well wires (CQWWs). The model of a cylindrical confining potential has the advantage to consider the finite width of the QWW in both spatial directions. Hence, this model is a good approximation for experimentally used QWWs in which the width of the confinement potential is nearly the same for both spatial directions. Further, the model of a CQWW allows in many cases to derive analytical expressions. The up to now obtained results on Q1D plasmons in CQWWs [22, 24] are restricted to the case that only the lowest subband is occupied, neglecting the effects of the image forces on the plasmons. Because of these restrictions the obtained results cannot explain the experiments in which mostly QWWs with many occupied subbands were used. The aim of this paper is to give a detailed investigation of Q1D plasmons in CQWWs in the case of one and two occupied subbands including the effect of the image potential. Experimental observations of Merkt [6] indicate the importance of the image contributions on the depolarization shift of the intersubband plasmons.

2. Ground State

We consider a CQWW in which the carriers are confined via a built-in local change in the crystal potential of the structure. It consists of a semiconductor material 1 embedded in a semiconductor of material 2, usually GaAs–$Ga_{1-x}Al_xAs$ or metal–oxide–semiconductor (MOS) structures on InSb with SiO_2 as the oxide. To describe the electrons in the conduction band of the host semiconductor, we use the effective-mass approximation.

In the model we use in this paper, we assume that the electrons are totally confined by the effective potential to move in a CQWW of radius R and are free to move along the axis of the wire of the length L_z which we assume to be the z-axis. Because translational symmetry in z-direction is assumed (Born-von Kármán boundary condition), the single-particle wave functions and the corresponding eigenvalues are

$$\langle \boldsymbol{x} \mid mlk_z \rangle = \psi_{mlk_z}(\boldsymbol{x}) = \frac{1}{\sqrt{L_z}} \mathrm{e}^{ik_z z} \phi_{ml}(r, \varphi), \tag{1}$$

$$\mathscr{E}_{ml}(k_z) = \mathscr{E}_{ml} + \frac{\hbar^2 k_z^2}{2m_e}, \tag{2}$$

where we use cylindrical coordinates (r, φ, z), suppose spin degeneracy, but omit the spin eigenvalue and coordinate. In the above equations m_e is the effective electron mass, k_z is the wave vector component in z-direction, and $\phi_{ml}(r, \varphi)$ and $\mathscr{E}_{ml}$ are obtained from the two-dimensional Schrödinger equation

$$\left[-\frac{\hbar^2}{2m_e} \left(\frac{1}{r} \frac{\partial}{\partial r} \left(r \frac{\partial}{\partial r} \right) + \frac{1}{r^2} \frac{\partial^2}{\partial \varphi^2} \right) + V_{\mathrm{eff}}(r) \right] \phi_{ml}(r, \varphi) = \mathscr{E}_{ml} \phi_{ml}(r, \varphi). \tag{3}$$

For the infinite cylindrical potential well, the wave function is given by

$$\phi_{ml}(r, \varphi) = \frac{1}{\sqrt{2\pi}} \mathrm{e}^{im\varphi} \varkappa_{ml}(r), \tag{4}$$

with

$$\varkappa_{ml}(r) = \sqrt{\frac{2}{R^2}} \frac{1}{\mathrm{J}_{|m|+1}(k_{|m|l} R)} \mathrm{J}_{|m|}(k_{|m|l} r), \tag{5}$$

and the corresponding energy is

$$\mathscr{E}_{ml} = \frac{\hbar^2 k_{|m|l}^2}{2m_e}. \tag{6}$$

Hence, the levels are twofold degenerated if $m \neq 0$. Here, $J_{|m|}(x)$ is the Bessel function of the order $|m|$, $m = 0, \pm 1, \pm 2, \ldots$ is the angular quantum number, $l = 1, 2, 3, \ldots$ is the radial quantum number (l is equally the number of the zeros of the radial wave function $\varkappa_{ml}(r)$ in the interval $[0, R]$) and $k_{|m|l}$ is related to the l-th root of the Bessel function of order $|m|$, i.e. $J_{|m|}(k_{|m|l}R) = 0$ resulting from the radial boundary condition $\psi_{mlk_z}(r = R, \varphi, z) = 0$. Thus the resulting subband ladder is $\varepsilon_{01} < \varepsilon_{11} < \varepsilon_{21} < \varepsilon_{02} < \varepsilon_{31} < \varepsilon_{12} < \varepsilon_{41} < \varepsilon_{03} < \ldots$. The Fermi energy is obtained from the condition

$$n_{1\mathrm{DEG}} = \frac{4}{\pi\hbar}\sqrt{\frac{m_e}{2}} \sum_{m=-\infty}^{\infty} \sum_{l=1}^{\infty} \sqrt{E_F - \mathscr{E}_{ml}}\, \theta(E_F - \mathscr{E}_{ml}), \tag{7}$$

with $n_{1\mathrm{DEG}}$ being the 1D electron number density (number of electrons per unit length) and $\theta(x)$ is the Heaviside unit step function ($\theta(x) = 1$ for $x > 0$ and $\theta(x) = 0$ for $x < 0$).

The goal of this paper is to calculate the density-response of a Q1DEG including the effect of the image potential on the collective excitations. Hence, to get a deeper insight we are interested to derive analytical results. As shown by Gold and Ghazali [24], the use of the following expressions of the normalized single-particle wave functions for the two lowest subbands:

$$\varkappa_{01}(r) = \frac{\sqrt{6}}{R}\left[1 - \left(\frac{r}{R}\right)^2\right], \tag{8}$$

$$\varkappa_{\pm 11}(r) = \frac{2\sqrt{6}}{R}\left(\frac{r}{R}\right)\left[1 - \left(\frac{r}{R}\right)^2\right], \tag{9}$$

results in good agreement with the exact result (5), if one calculates the bare electron–electron interaction potential. Here we will use these wave functions.

3. Density Response of a Q1DEG

In this chapter we calculate the response of a Q1DEG to an external potential on a quantum-mechanical level within the RPA, also known as the *time-dependent Hartree method*. Here we use the *self-consistent field* (SCF) method of Ehrenreich and Cohen [44].

The single-particle Hamiltonian of the electrons of the Q1DEG in the presence of the perturbation is written as $H = H_0 + H_1$, where H_0 is the unperturbed Hamiltonian of a single electron in the CQWW which satisfies the Schrödinger equation $H_0 |m, l, k_z\rangle = \mathscr{E}_{ml}(k_z) |m, l, k_z\rangle$ and $H_1 = V^{sc}(\boldsymbol{x}, t)$ is the *self-consistent potential*. The single-particle von Neumann equation for the statistical operator ϱ_G describing the response of the system to the self-consistent potential, can be linearized with $\varrho_G = \varrho_G^{(0)} + \varrho_G^{(1)}$, where $\varrho_G^{(0)}$ is the statistical operator of the unperturbed system, and $\varrho_G^{(1)}$ is the correction to the statistical

operator to the first order in the perturbation. Retaining only the linear terms in the single-particle von Neumann equation, we obtain

$$i\hbar \frac{\partial}{\partial t} \varrho_G^{(1)} = [H_0, \varrho_G^{(1)}] + [H_1, \varrho_G^{(0)}]. \tag{10}$$

The external potential is adiabatically switched on at $t = -\infty$ giving $V^{ext}(x, t) = V^{ext}(x, \omega) \exp[-i(\omega + i\delta) t]$ with $\delta \to 0^+$. This time dependence is assumed for all the potentials and the steady-state properties of the system are evaluated at $t = 0$. Using a general state $|\nu\rangle$ of the unperturbed system, where $\{\nu\}$ stands for $\{m, l, k_z\}$, we find by evaluating (10) between states $|\nu\rangle$ and $|\nu'\rangle$

$$\langle \nu | \varrho_G^{(1)} | \nu' \rangle = \frac{n_F(\mathscr{E}_{\nu'}) - n_F(\mathscr{E}_\nu)}{\hbar(\omega + i\delta) + \mathscr{E}_{\nu'} - \mathscr{E}_\nu} \langle \nu | V^{sc}(x, \omega) | \nu' \rangle, \tag{11}$$

where $\varrho_G^{(0)} |\nu\rangle = n_F(\mathscr{E}_\nu) |\nu\rangle$ is used with $n_F(\mathscr{E}_\nu) = \theta(E_F - \mathscr{E}_\nu)$ the Fermi distribution function at $T = 0$ K.

In the next step of the SCF method we have to calculate the electron number density n_{ind} of the Q1DEG, induced by the external potential V^{ext}. The total electron number density $n = n_0 + n_{ind}$ of the Q1DEG, with n_0 the ground-state electron number density, is given by $n(x, \omega) = \mathrm{Tr}\{\varrho_G \delta(x - x_e)\}$. The induced electron number density, $n_{ind}(x, \omega) = \mathrm{Tr}\{\varrho_G^{(1)} \delta(x - x_e)\}$, is calculated to be

$$n_{ind}(x, \omega) = \int d^3x' P^{(1)}(x, x' | \omega) V^{sc}(x', \omega), \tag{12}$$

where $P^{(1)}(x, x' | \omega)$ is the *irreducible RPA polarization function* of the Q1DEG

$$P^{(1)}(x, x' | \omega) = \sum_{\nu\nu'} \frac{n_F(\mathscr{E}_{\nu'}) - n_F(\mathscr{E}_\nu)}{\hbar(\omega + i\delta) + \mathscr{E}_{\nu'} - \mathscr{E}_\nu} \psi_\nu(x) \psi_\nu^*(x') \psi_{\nu'}(x') \psi_{\nu'}^*(x). \tag{13}$$

The *self-consistent potential* $V^{sc}(x, \omega)$ is composed of the *external potential* $V^{ext}(x, \omega)$ and the *induced potential* $V^{ind}(x, \omega)$, which arises from the change in the carrier density induced by the external potential. According to the spatial symmetry of the problem we introduce one-dimensional Fourier series

$$V^{sc}(x, \omega) = \frac{1}{L_z} \sum_{q_z} e^{iq_z z} V^{sc}(x_\perp; q_z | \omega), \tag{14}$$

$$V^{sc}(x_\perp; q_z | \omega) = \int dz\, e^{-iq_z z} V^{sc}(x, \omega) \tag{15}$$

with $x_\perp = xe_x + ye_y = re_r$.

In the next step we have to calculate the self-consistent potential induced by the redistributed charges using electrodynamics. In the RPA and neglecting retardation effects the induced potential is related to the induced density by Poisson's equation, which reads for a QWW

$$[\nabla x_\perp \varepsilon_s(x_\perp) \nabla x_\perp - \varepsilon_s(x_\perp) q_z^2] \phi^{ind}(x_\perp; q_z | \omega) = -\frac{1}{\varepsilon_0} \varrho^{ind}(x_\perp; q_z | \omega). \tag{16}$$

Herein, ϕ^{ind} is the *induced scalar potential* and $V^{ind} = -e\phi^{ind}$ is valid for an electron in the presence of ϕ^{ind}, $\varrho^{ind} = -en_{ind}$ is the *induced electron charge density* and $\varepsilon_s(x_\perp)$ is the

static dielectric function of the semiconductor background arising from the high-energy electronic excitations across the band gap and the optical phonons. This is true because the frequencies of the optical phonons are usually larger than those of the plasmons of the Q1DEG [29]. Hence, the ε_s-*approximation* for the *screening* of the background gives excellent results and is used throughout this paper. $\varepsilon_s(\boldsymbol{x}_\perp)$ is a constant in each semiconductor: $\varepsilon_s(\boldsymbol{x}_\perp) = \varepsilon_{s1}$ for $r \leqq R$, and $\varepsilon_s(\boldsymbol{x}_\perp) = \varepsilon_{s2}$ for $r > R$. It is convenient to solve Poisson's equation with the help of the Green's function $D(\boldsymbol{x}, \boldsymbol{x}')$. This Green's function describes the electrostatic problem for the non-magnetic background semiconductor characterized by the dielectric function $\varepsilon_s(\boldsymbol{x}_\perp)$, without the Q1DEG. It satisfies the boundary conditions at $r = R$ and $r = \infty$ and is calculated in Appendix A. For inhomogeneous systems in which the materials have different but constant polarizabilities, the Green's function of the Poisson equation contains two parts, the *direct Coulomb part*, D^{dir}, and the *image part*, D^{im}. The formal solution for the induced scalar potential is

$$\phi^{\mathrm{ind}}(\boldsymbol{x}_\perp; q_z \mid \omega) = \frac{1}{\varepsilon_0} \int \mathrm{d}^2 x'_\perp \, D(\boldsymbol{x}_\perp, \boldsymbol{x}'_\perp; q_z) \, \varrho^{\mathrm{ind}}(\boldsymbol{x}'_\perp; q_z \mid \omega) \,. \tag{17}$$

Using (12) in the formal solution of Poisson's equation (17), we obtain the self-consistent potential

$$V^{\mathrm{sc}}(\boldsymbol{x}_\perp; q_z \mid \omega) = V^{\mathrm{ext}}(\boldsymbol{x}_\perp; q_z \mid \omega) + \frac{e^2}{\varepsilon_0} \int \mathrm{d}^2 x'_\perp \int \mathrm{d}^2 x''_\perp \, D(\boldsymbol{x}_\perp, \boldsymbol{x}'_\perp; q_z) \times P^{(1)}(\boldsymbol{x}'_\perp, \boldsymbol{x}''_\perp; q_z \mid \omega) \, V^{\mathrm{sc}}(\boldsymbol{x}''_\perp; q_z \mid \omega) \,. \tag{18}$$

From this equation one obtains the condition for the existence of the collective excitations of the Q1DEG under the assumption that a finite self-consistent potential exists, $V^{\mathrm{sc}} \neq 0$, with no applied external potential, $V^{\mathrm{ext}} = 0$. This existence condition reads

$$V^{\mathrm{sc}}(\boldsymbol{x}_\perp; q_z \mid \omega) = \frac{e^2}{\varepsilon_0} \int \mathrm{d}^2 x'_\perp \int \mathrm{d}^2 x''_\perp \, D(\boldsymbol{x}_\perp, \boldsymbol{x}'_\perp; q_z) \, P^{(1)}(\boldsymbol{x}'_\perp, \boldsymbol{x}''_\perp; q_z \mid \omega) \, V^{\mathrm{sc}}(\boldsymbol{x}''_\perp; q_z \mid \omega) \,. \tag{19}$$

Now we use the wave functions (1) and subband energies (2) of noninteracting electrons in the CQWW. We obtain for the RPA polarization function

$$P^{(1)}(\boldsymbol{x}, \boldsymbol{x}' \mid \omega) = \frac{1}{L_z} \sum_{q_z = -\infty}^{\infty} \mathrm{e}^{\mathrm{i}q_z(z - z')} \, P^{(1)}(\boldsymbol{x}_\perp, \boldsymbol{x}'_\perp; q_z \mid \omega) \,, \tag{20}$$

with

$$P^{(1)}(\boldsymbol{x}_\perp, \boldsymbol{x}'_\perp; q_z \mid \omega) = P^{(1)}(r, r'; \varphi - \varphi'; q_z \mid \omega) = \frac{1}{2\pi} \sum_{n = -\infty}^{\infty} \mathrm{e}^{\mathrm{i}n(\varphi - \varphi')} \times P_n^{(1)}(r, r'; q_z \mid \omega) \,, \tag{21}$$

$$P_n^{(1)}(r, r'; q_z \mid \omega) = \sum_{m = -\infty}^{\infty} \sum_{l, l' = 1}^{\infty} P^{(1)}_{\substack{m+n\,m \\ l\quad l'}}(q_z, \omega) \, \eta_{\substack{m+n\,m \\ l\quad l'}}(r) \, \eta^*_{\substack{m+n\,m \\ l\quad l'}}(r') \,, \tag{22}$$

$$P^{(1)}_{\substack{m+n\,m \\ l\quad l'}}(q_z, \omega) = \frac{1}{\pi L_z} \sum_{k_z = -\infty}^{\infty} \frac{n_{\mathrm{F}}(\mathscr{E}_{ml'}(k_z)) - n_{\mathrm{F}}(\mathscr{E}_{m+n\,l}(k_z + q_z))}{\hbar(\omega + \mathrm{i}\delta) + \mathscr{E}_{ml'}(k_z) - \mathscr{E}_{m+n\,l}(k_z + q_z)} \tag{23}$$

and

$$\eta_{\substack{m+n\,m\\ l\quad l'}}(r) = \varkappa_{m+n\,l}(r)\,\varkappa^{*}_{ml'}(r)\,. \tag{24}$$

Within the RPA and for $T = 0\,\mathrm{K}$ the matrix polarization function $P^{(1)}_{\substack{m+n\,m\\ l\quad l'}}(q_z, \omega)$ of the Q1DEG in the CQWW is [29]

$$\begin{aligned}\operatorname{Re} P^{(1)}_{\substack{m+n\,m\\ l\quad l'}}(q_z, \omega) = -\frac{m_e}{2\pi^2\hbar^2 q_z}\Bigg[\ln\left|\frac{k_F^{ml'} + q_z/2 - (m_e/\hbar q_z)\left(\omega - \Omega_{\substack{m+n\,m\\ l\quad l'}}\right)}{k_F^{ml'} - q_z/2 + (m_e/\hbar q_z)\left(\omega - \Omega_{\substack{m+n\,m\\ l\quad l'}}\right)}\right| \\ + \ln\left|\frac{k_F^{m+n\,l} + q_z/2 + (m_e/\hbar q_z)\left(\omega - \Omega_{\substack{m+n\,m\\ l\quad l'}}\right)}{k_F^{m+n\,l} - q_z/2 - (m_e/\hbar q_z)\left(\omega - \Omega_{\substack{m+n\,m\\ l\quad l'}}\right)}\right| \Bigg],\end{aligned} \tag{25}$$

where $k_F^{ml} = [2m_e(E_F - \mathscr{E}_{ml})/\hbar^2]^{1/2}$ if $E_F > \mathscr{E}_{ml}$ and zero for $E_F \leqq \mathscr{E}_{ml}$ and $\Omega_{\substack{m\,m'\\ l\quad l'}} = (\mathscr{E}_{ml} - \mathscr{E}_{m'l'})/\hbar$ is the subband separation frequency. The imaginary part of the matrix polarization function is given by [29]

$$\begin{aligned}\operatorname{Im} P^{(1)}_{\substack{m+n\,m\\ l\quad l'}}(q_z, \omega) = -\frac{m_e}{2\pi\hbar^2|q_z|}\Bigg\{\theta\left[k_F^{ml'} + \frac{q_z}{2} - \frac{m_e}{\hbar q_z}\left(\omega - \Omega_{\substack{m+n\,m\\ l\quad l'}}\right)\right] \\ \times\theta\left[k_F^{ml'} - \frac{q_z}{2} + \frac{m_e}{\hbar q_z}\left(\omega - \Omega_{\substack{m+n\,m\\ l\quad l'}}\right)\right] \\ - \theta\left[k_F^{m+n\,l} + \frac{q_z}{2} + \frac{m_e}{\hbar q_z}\left(\omega - \Omega_{\substack{m+n\,m\\ l\quad l'}}\right)\right] \\ \times\theta\left[k_F^{m+n\,l} - \frac{q_z}{2} - \frac{m_e}{\hbar q_z}\left(\omega - \Omega_{\substack{m+n\,m\\ l\quad l'}}\right)\right]\Bigg\}.\end{aligned} \tag{26}$$

The matrix polarization functions given in (25) and (26) have the symmetry properties

$$P^{(1)}_{\substack{m\,m'\\ l\quad l'}}(q_z, \omega) = P^{(1)}_{\substack{m\,m'\\ l\quad l'}}(-q_z, \omega)\,, \qquad \operatorname{Re} P^{(1)}_{\substack{m\,m'\\ l\quad l'}}(q_z, \omega) = \operatorname{Re} P^{(1)}_{\substack{m'\,m\\ l'\quad l}}(q_z, -\omega),$$

$$\operatorname{Im} P^{(1)}_{\substack{m\,m'\\ l\quad l'}}(q_z, \omega) = -\operatorname{Im} P^{(1)}_{\substack{m'\,m\\ l'\quad l}}(q_z, -\omega),$$

and $P^{(1)}_{\substack{m\,m'\\ l\quad l'}}(q_z, \omega) = 0$ if both $\mathscr{E}_{ml} > E_F$ and $\mathscr{E}_{m'l'} > E_F$ are valid. Using (21) to (24) for the polarization function and

$$D(\boldsymbol{x}_\perp, \boldsymbol{x}'_\perp; q_z) = D(r, r'; \varphi - \varphi'; q_z) = \frac{1}{2\pi}\sum_{n'=-\infty}^{\infty} \mathrm{e}^{\mathrm{i}n'(\varphi-\varphi')}\, D_{n'}(r, r'; q_z)$$

in the existence condition (19) we obtain after performing matrix elements

$$\begin{aligned}&\sum_{m=-\infty}^{\infty}\sum_{l,l'=1}^{\infty}\left[\delta_{m\,m_1-n}\delta_{ll_1}\delta_{l'l_2} - V^{s}_{\substack{m_1\,m_1-n\,m\,m+n(q_z)\\ l_1\quad l_2\quad l'\quad l}} P^{(1)}_{\substack{m+n\,m\\ l\quad l'}}(q_z, \omega)\right] \\ &\times V^{sc}_{\substack{m+n\,m\\ l\quad l'}}(q_z, \omega) = 0\,.\end{aligned} \tag{27}$$

Herein $V^{s}_{\substack{m_1 m_2 m_3 m_4 \\ l_1 l_2 l_3 l_4}}(q_z)$ is the matrix element of the Coulomb potential

$$V^{s}_{\substack{m_1 m_2 m_3 m_4 \\ l_1 l_2 l_3 l_4}}(q_z) = \frac{e^2}{\varepsilon_0}\left[\int_0^R \mathrm{d}r\, r \int_0^R \mathrm{d}r'\, r' \eta^{*}_{\substack{m_1 m_2 \\ l_1 l_2}}(r)\, D_n(r, r'; q_z)\, \eta^{*}_{\substack{m_3 m_4 \\ l_3 l_4}}(r')\right]$$

$$\times \delta_{m_2 m_1 - n}\delta_{m_4 m_3 + n} = \frac{e^2}{e_0 \varepsilon_{s1}} f^{C}_{\substack{m_1 m_2 m_3 m_4 \\ l_1 l_2 l_3 l_4}}(q_z)\, \delta_{m_2 m_1 - n}\delta_{m_4 m_3 + n}\,, \quad (28)$$

where $f^{C}_{\substack{m_1 m_2 m_3 m_4 \\ l_1 l_2 l_3 l_4}}(q_z)$ is the form factor. The conditions $m_2 = m_1 - n$ and $m_4 = m_3 + n$ follow from the axial symmetry of the cylindrical potential. The matrix element signifies the scattering of an electron from the subband $(m_2 l_2)$ to $(m_1 l_1)$ by another electron which becomes scattered from $(m_4 l_4)$ to $(m_3 l_3)$. Further, we have defined

$$V^{sc}_{\substack{m_1 m_2 \\ l_1 l_2}}(q_z, \omega) = \left[\int_0^R \mathrm{d}r\, r\, \eta^{*}_{\substack{m_1 m_2 \\ l_1 l_2}} V^{sc}_n(r, q_z \mid \omega)\right] \delta_{m_1 m_2 + n}$$

$$= f^{sc}_{\substack{m_1 m_2 \\ l_1 l_2}}(q_z, \omega)\, \delta_{m_1 m_2 + n}\,, \quad (29)$$

where $V^{sc}_n(r, q_z \mid \omega)$ is the Fourier transform of the screened potential $V^{sc}(r, \varphi)$ analogous to (21). The axial symmetry of the cylindrical wire results in $n = m_1 - m_2$. The system of equations (27) is identical $n \geqq 0$ and $n \leqq 0$. In the following we therefore restrict to the case $n \geqq 0$ without loss of generality.

According to the symmetry of the Green's function, $D_n(r, r'; q_z) = D_n(r', r; q_z)$, and the reality of the radial wave functions we have: $f^{C}_{\substack{m_1 m_2 m_3 m_4 \\ l_1 l_2 l_3 l_4}} = f^{C}_{\substack{m_2 m_1 m_3 m_4 \\ l_2 l_1 l_3 l_4}} = f^{C}_{\substack{m_1 m_2 m_4 m_3 \\ l_1 l_2 l_4 l_3}}$ $= f^{C}_{\substack{m_3 m_4 m_1 m_2 \\ l_3 l_4 l_1 l_2}}$ and $f^{sc}_{\substack{m_1 m_2 \\ l_1 l_2}} = f^{sc}_{\substack{m_2 m_1 \\ l_2 l_1}}$. Using these symmetries and the symmetries of the matrix polarization function in (27), we obtain for the existence condition of collective excitations the following equation:

$$\sum_{m \geqq -[n/2]}^{\infty} \sum_{l, l' = 1}^{\infty} \left[\delta_{m m_1 - n}\delta_{l l_1}\delta_{l' l_2} - V^{s}_{\substack{m_1 m_1 - n\, m m + n \\ l_1 l_2 l' l}}(q_z)\, \chi^{(1)}_{\substack{m+n\, m \\ l\, l'}}(q_z, \omega)\right]$$

$$\times V^{sc}_{\substack{m+l\, m \\ l\, l'}}(q_z, \omega) = 0 \quad (30)$$

with

$$\chi^{(1)}_{\substack{m+n\, m \\ l\, l'}}(q_z, \omega) = \begin{cases} P^{(1)}_{\substack{m+n\, m \\ l\, l'}}(q_z, \omega) + P^{(1)}_{\substack{m\, m+n \\ l'\, l}}(q_z, \omega) & \text{if} \quad m \neq -\left[\dfrac{n}{2}\right], \\ P^{(1)}_{\substack{n/2\, n/2 \\ l\, l'}}(q_z, \omega) & \text{if} \quad m = -\dfrac{n}{2}. \end{cases} \quad (31)$$

In (30) and (31) $[n/2]$ signifies the integral part of $n/2$. The matrix polarization function $\chi^{(1)}_{\substack{m\, m' \\ l\, l'}}(q_z, \omega)$ contains two physically different contributions:

(i) the intrasubband contribution for $m = m'$ and $l = l'$ arising from electron excitations above the Fermi surface within one occupied subband and

(ii) the intersubband contribution for $m \neq m'$ and $l \neq l'$, or $m \neq m'$ and $l = l'$, or $m = m'$ and $l \neq l'$ arising from electron excitations above the Fermi surface between different subbands.

The dispersion relation of the collective excitations of the Q1DEG in the CQWW, the intra- and intersubband plasmons, follows from (30) under the condition that this system of algebraic equations has nontrivial solutions $V^{\mathrm{sc}}_{\substack{m+n\,m\\ l\ \ l'}}$. Then the dispersion relation reads

$$\det\left[\delta_{m\,m_1-n}\delta_{l l_1}\delta_{l' l_2} - V^{\mathrm{s}}_{\substack{m_1\ m_1-n\ m\ m+n\\ l_1\ \ l_2\ \ l'\ \ l}}(q_z)\,\chi^{(1)}_{\substack{m+n\,m\\ l\ \ l'}}(q_z,\omega)\right] = 0 \tag{32}$$

determining the eigenfrequencies of the Q1D plasmons. We denote each branch with $\omega_{\mathrm{p}}{}^{\substack{m+n\,m\\ l\ \ l'}}$. The symmetry of the CQWW causes that Q1D plasmon branches $\omega_{\mathrm{p}}{}^{\substack{m+n\,m\\ l\ \ l'}}$ which are connected with the collective electron transition between subbands with equal difference between the two angular quantum numbers ($m \to m + n$) are coupled modes but are decoupled from such branches which have a different difference Δm of the two angular quantum numbers. That means that the plasmons form groups of coupled modes: $n = 0$: $\omega_{\mathrm{p}}^{00}, \omega_{\mathrm{p}}^{11}, \omega_{\mathrm{p}}^{22}, \ldots$; $n = 1$: $\omega_{\mathrm{p}}^{10}, \omega_{\mathrm{p}}^{21}, \omega_{\mathrm{p}}^{32}, \ldots$; $n = 2$: $\omega_{\mathrm{p}}^{20}, \omega_{\mathrm{p}}^{31}, \omega_{\mathrm{p}}^{42}, \ldots$; ... with coupling between the branches of one certain group but without coupling between the branches of the different groups concerning different n.

4. Coulomb Potential

In this section we discuss the Coulomb potential which is a sum of the direct Coulomb potential and the image potential

$$V^{\mathrm{s}}_{\substack{m_1\ m_2\ m_3\ m_4\\ l_1\ \ l_2\ \ l_3\ \ l_4}}(q_z) = V^{\mathrm{dir}}_{\substack{m_1\ m_2\ m_3\ m_4\\ l_1\ \ l_2\ \ l_3\ \ l_4}}(q_z) + V^{\mathrm{im}}_{\substack{m_1\ m_2\ m_3\ m_4\\ l_1\ \ l_2\ \ l_3\ \ l_4}}(q_z)\,, \tag{33}$$

with

$$V^{\mathrm{dir}}_{\substack{m_1\ m_2\ m_3\ m_4\\ l_1\ \ l_2\ \ l_3\ \ l_4}}(q_z) = \frac{e^2}{\varepsilon_0}\int_0^R \mathrm{d}r\, r \int_0^R \mathrm{d}r'\, r' \eta^*_{\substack{m_1\ m_2\\ l_1\ \ l_2}}(r)\, D_n^{\mathrm{dir}}(r, r'; q_z)\, \eta^*_{\substack{m_3\ m_4\\ l_3\ \ l_4}}(r') \tag{34}$$

and

$$V^{\mathrm{im}}_{\substack{m_1\ m_2\ m_3\ m_4\\ l_1\ \ l_2\ \ l_3\ \ l_4}}(q_z) = \frac{e^2}{\varepsilon_0}\int_0^R \mathrm{d}r\, r \int_0^R \mathrm{d}r'\, r' \eta^*_{\substack{m_1\ m_2\\ l_1\ \ l_2}}(r)\, D_n^{\mathrm{im}}(r, r'; q_z)\, \eta^*_{\substack{m_3\ m_4\\ l_3\ \ l_4}}(r')\,. \tag{35}$$

$D_n^{\mathrm{dir}}(r, r'; q_z)$ and $D_n^{\mathrm{im}}(r, r'; q_z)$ are given in Appendix A. Unfortunately, it is impossible to get analytical results for $V^{\mathrm{s}}_{\substack{m_1\ m_2\ m_3\ m_4\\ l_1\ \ l_2\ \ l_3\ \ l_4}}(q_z)$ if one uses the wave functions given in (4) and (5). In order to get analytical results for the Coulomb potential, we use the approximate wave functions of (8) and (9). The explicit results for $V^{\mathrm{dir}}_{\substack{m_1\ m_2\ m_3\ m_4\\ l_1\ \ l_2\ \ l_3\ \ l_4}}(q_z)$ and $V^{\mathrm{im}}_{\substack{m_1\ m_2\ m_3\ m_4\\ l_1\ \ l_2\ \ l_3\ \ l_4}}(q_z)$ are given in Appendix B. Because within this two-subband model the subband indices l_1, l_2, l_3, l_4 remain always fixed at "1" we omit these in the following.

Most experiments on QWWs are done for the system GaAs–$Ga_{1-x}Al_xAs$ and the InSb–MOS system. The material constants for GaAs in which the Q1DEG is synthesized are: $\varepsilon_{\mathrm{s}1} = 12.87$ and $m_{\mathrm{e}} = 0.06624\,m_0$ and for AlAs: $\varepsilon_{\mathrm{s}2} = 10.22$. For InSb is valid: $\varepsilon_{\mathrm{s}1} = 17.88$ and $m_{\mathrm{e}} = 0.0139\,m_0$ and for SiO_2: $\varepsilon_{\mathrm{s}2} = 3.8$.

In Fig. 1 the ratio $V^{\mathrm{dir}}_{m_1m_2m_3m_4}/(V^{\mathrm{dir}}_{m_1m_2m_3m_4} + V^{\mathrm{im}}_{m_1m_2m_3m_4})$ for the different matrix elements of the Coulomb potential is plotted. The different curves correspond to different values of the parameter $\xi = 1 - \varepsilon_{\mathrm{s}2}/\varepsilon_{\mathrm{s}1}$. We notice that the curve with $\xi = 0.21$ corresponds to the

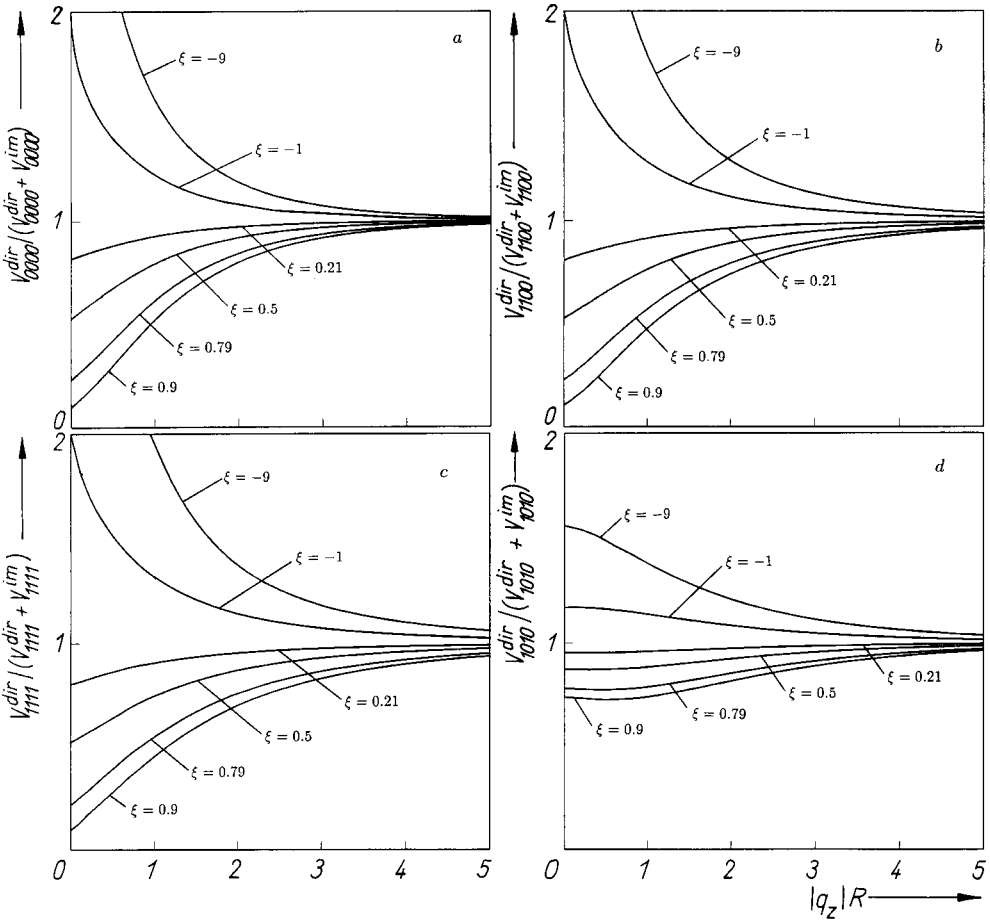

Fig. 1. The ratio $V^{dir}_{m_1m_2m_3m_4}/(V^{dir}_{m_1m_2m_3m_4} + V^{im}_{m_1m_2m_3m_4})$ of the different matrix elements of the Coulomb potential for a CQWW as a function of $|q_z|\,R$ for different values of $\xi = 1 - \varepsilon_{s2}/\varepsilon_{s1}$

GaAs–AlAs QWW and that with $\xi = 0.79$ to the InSb–MOS QWW. It is shown that the image effects increase with decreasing $|q_z|\,R$ and increasing $|\xi|$. Image effects become important for the electron–electron interaction if $|q_z|\,R \leqq 1$. In this region the contribution of the image effects to the Coulomb interaction is more than 10%. For very small values of $|q_z|\,R$ the matrix element V^{s}_{1010} is less influenced by image effects than the other one.

5. Collective Excitations

To solve the complicated algebraic equation which determines the dispersion relation of the collective excitations it is necessary to restrict the discussion to a finite number of subbands. Because throughout this paper we are interest in analytical results, we use the two-subband model ($m = 0, 1; l = 1$). In two recent papers [29, 30] we calculated numerically the dispersion relation of the collective excitation for a multi-subband model. The reader who is interested in effects caused by many subbands is directed to these references. Further

we use the matrix elements of the Coulomb potential (B1) to (B8), calculated with the approximated wave functions of (8) and (9). The spatial symmetry of the CQWW guarantees that the dispersion relation of our model splits into two separate ones. One describes the modes for $n = 0$ and follows from (32)

$$[1 - V^{s}_{0000}(q_z)\,\chi^{(1)}_{00}(q_z, \omega)]\,[1 - V^{s}_{1111}(q_z)\,\chi^{(1)}_{11}(q_z, \omega)] - V^{s}_{1100}(q_z)\,V^{s}_{0011}(q_z)\,\chi^{(1)}_{00}(q_z, \omega)\,\chi^{(1)}_{11}(q_z, \omega) = 0\,. \tag{36}$$

The second equation follows for $n = 1$ from (32)

$$1 - V^{s}_{1010}(q_z)\,\chi^{(1)}_{10}(q_z, \omega) = 0\,. \tag{37}$$

If only one subband is occupied, $\chi^{(1)}_{11}(q_z, \omega) = 0$ and (36) describes the pure intrasubband plasmon of the lower subband. If two subbands are occupied, the intrasubband plasmons of the two occupied subbands are coupled modes. For the two-subband model the modes with $n = 1$ are pure intersubband plasmons.

5.1 One subband is occupied

5.1.1 Intrasubband plasmons

In the two-subband model assuming at first that only one subband is occupied, i.e. in the *electric quantum limit* (EQL), the dispersion relation of the intrasubband plasmons reads

$$1 - V^{s}_{0000}(q_z)\,\chi^{(1)}_{00}(q_z, \omega) = 0\,. \tag{38}$$

Because the investigation of the Coulomb potential in the last section shows that the effect of the image potential for the GaAs–AlAs QWW is much weaker than for the InSb–MOS QWW we restrict the discussion on the last system.

In Fig. 2 the full RPA dispersion curves of the intrasubband plasmons are plotted including the image potential (solid line) and neglecting the image potential (dashed line). The shaded area in the $\omega - q_z$ plane is the region where the single-particle intrasubband excitations

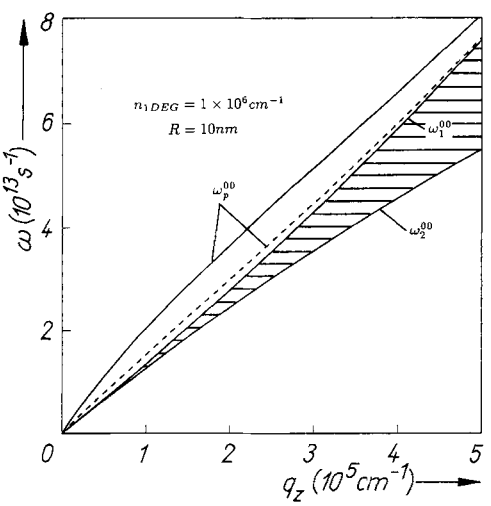

Fig. 2. Dispersion relation of the intrasubband plasmon of an InSb–MOS CQWW where one subband is occupied. The dispersion curve calculated including image effects is given by the solid line and without image effects by the dashed line. The shaded area corresponds to the single-particle intrasubband continuum (Im $\chi^{(1)}_{00}(q_z, \omega) \neq 0$) with the boundaries: $\omega_1^{00} = (\hbar k_F^{01}/m_e)\,q_z + (\hbar/2m_e)\,q_z^2$, $\omega_2^{00} = |-(\hbar k_F^{01}/m_e) \times q_z + (\hbar/2m_e)\,q_z^2|$

exist. In this region $\operatorname{Im} \chi_{00}^{(1)}(q_z, \omega) \neq 0$ and the collective excitations are Landau damped. The dispersion curves of the intrasubband plasmons start at $q_z = 0$ and $\omega = 0$ and approach for large wave vectors the boundary ω_1^{00} of the single-particle intrasubband continuum. We note that according to the logarithmic divergency of $\chi_{00}^{(1)}(q_z, \omega)$ at the boundary ω_1^{00} the dispersion curves do not cross this boundary. It is shown that the image contribution to the Coulomb interaction results in an enhancement of the frequency of the intrasubband plasmon. For the chosen CQWWs with $R = 10$ nm and $n_{1\mathrm{DEG}} = 1 \times 10^6\ \mathrm{cm}^{-1}$, the shift of the dispersion curves caused by image effects is for $q_z = 1 \times 10^4\ \mathrm{cm}^{-1}$ 50.5%, for $q_z = 1 \times 10^5\ \mathrm{cm}^{-1}$ 33%, and for $q_z = 5 \times 10^5\ \mathrm{cm}^{-1}$ 8%.

In the limit of small wave vectors, if $\hbar k_{\mathrm{F}}^{01} |q_z|$, $\hbar q_z^2/2 \ll m_e \omega$ is valid, it follows for the matrix polarization function

$$P_{00}^{(1)}(q_z, \omega) = \frac{n_{1\mathrm{DEG}} q_z^2}{2\pi m_e \omega^2} \left\{ 1 + \frac{\hbar^2 q_z^2}{m_e^2 \omega^2} \left[(k_{\mathrm{F}}^{01})^2 + \frac{q_z^2}{4} \right] + O\left[\left(\frac{\hbar q_z}{m_e \omega} \left(k_{\mathrm{F}}^{01} + \frac{\hbar |q_z|}{2m_e} \right) \right)^4 \right] \right\}, \tag{39}$$

with $n_{1\mathrm{DEG}} = 2k_{\mathrm{F}}^{01}/\pi$ for one occupied subband. Using (39) in the dispersion relation (38), we obtain for the dispersion relation of the intrasubband plasmon

$$\omega_{\mathrm{p}}^{00} = \omega_{\mathrm{s}1} |q_z| R \left\{ \frac{f_{0000}^{\mathrm{C}}(q_z)}{2} \left[1 + \sqrt{1 + \frac{4[(v_{\mathrm{F}}^{01})^2 + \hbar^2 q_z^2/4m_e^2]}{(\omega_{\mathrm{s}1} R)^2 f_{0000}^{\mathrm{C}}(q_z)}} \right] \right\}^{1/2}, \tag{40}$$

with

$$\omega_{\mathrm{s}1} = \left(\frac{n_{1\mathrm{DEG}} e^2}{2\pi \varepsilon_0 \varepsilon_{\mathrm{s}1} m_e R^2} \right)^{1/2} \tag{41}$$

and the Fermi velocity $v_{\mathrm{F}}^{01} = \hbar k_{\mathrm{F}}^{01}/m_e$. In the lowest order of $|q_z| R$ of (B9) and (B10) the dispersion relation of the intrasubband plasmon reads

$$\omega_{\mathrm{p}}^{00} = \omega_{\mathrm{s}2} |q_z| R \left[-\ln (|q_z| R) \right]^{1/2}, \tag{42}$$

where now

$$\omega_{\mathrm{s}2} = \left(\frac{n_{1\mathrm{DEG}} e^2}{2\pi \varepsilon_0 \varepsilon_{\mathrm{s}2} m_e R^2} \right)^{1/2}. \tag{43}$$

Hence, the plasmon is screened by the surrounding medium. This is true because for small wave vectors the image field is well extended in radial direction. This implies that the Coulomb interaction is mainly screened by the surrounding medium. For a small radius of the CQWW nearly all field lines of the Coulomb interaction are within the surrounding medium. Neglecting image effects one obtains in the long-wavelength limit the uncorrect result that the Coulomb interaction is screened by the background dielectric constant $\varepsilon_{\mathrm{s}1}$ of the host material and hence, the uncorrect result $\omega_{\mathrm{p}}^{00} = \omega_{\mathrm{s}1} |q_z| R \left[-\ln (|q_z| R) \right]^{1/2}$ for the intrasubband plasmon is obtained.

In the next order of $|q_z| R$, and using the first-order term of (39), the dispersion relation reads

$$\omega_{\mathrm{p}}^{00} = \omega_{\mathrm{s}2} |q_z| R \left[-\ln \left(\frac{\gamma |q_z| R}{2} \right) + 0.6083 \frac{\varepsilon_{\mathrm{s}2}}{\varepsilon_{\mathrm{s}1}} \right]^{1/2}. \tag{44}$$

Unfortunately, the condition $v_F^{01}|q_z| \ll \omega$ for the validity of the expansion of $\chi_{00}^{(1)}(q_z, \omega)$, in (39), is mostly not fulfilled in the experimentally realized QWWs. For instance, for the here chosen values of $R = 10$ nm and $n_{1\,DEG} = 1 \times 10^6\ cm^{-1}$, this condition is not fulfilled for $q_z \geqq 0.1\ cm^{-1}$. Further, it would be valid in the typical experimental range of $q_z \approx 10^5\ cm^{-1}$ only for $n_{1\,DEG} \leqq 1 \times 10^4\ cm^{-1}$, which is unrealistically small. Hence, in general only for very low densities $n_{1\,DEG}$ this condition is realized. In the following, we have to look for an expansion of $x_{00}^{(1)}(q_z, \omega)$ in a power series valid for larger electron densities and wave vectors. For wave vectors $|q_z|/2 \ll k_F^{01} - m_e\omega/\hbar|q_z| < k_F^{01} + m_e\omega/\hbar|q_z|$ we obtain

$$P_{00}^{(1)}(q_z, \omega) = \frac{m_e}{\pi^2\hbar^2} \frac{k_F^{01}}{[(m_e\omega/\hbar q_z)^2 - (k_F^{01})^2]} \left\{1 + \frac{[(k_F^{01})^2 + 3(m_e\omega/\hbar q_z)^2]\, q_z^2}{12[(k_F^{01})^2 - (m_e\omega/\hbar q_z)^2]^2} + O\left[\frac{1}{8}\left|k_F^{01} - \frac{m_e\omega}{\hbar|q_z|}\right|^{-3} |q_z|^3\right]\right\}. \tag{45}$$

Using (45) in (38) we obtain for dispersion relations of the intrasubband plasmons in the lowest order of $|q_z|\,R$

$$\omega_p^{00} = |q_z|\,R\left[\left(\frac{v_F^{01}}{R}\right)^2 - \omega_{s2}^2 \ln(|q_z|\,R)\right]^{1/2}. \tag{46}$$

This long-wavelength approximation is valid for larger $n_{1\,DEG}$, q_z, and R as (40) and (41). By $n_{1\,DEG}$, q_z, $R \to 0$ (46) turns into (42). It is noticeable that the above long-wavelength expression of the RPA dispersion relation is exactly the same as the dispersion relation of the elementary excitation of the Tomonaga-Luttinger model [45, 46] which is an exact solution of this model.

In the next order of $|q_z|\,R$ (46) reads

$$\omega_p^{00} = |q_z|\,R\left\{\left(\frac{v_F^{01}}{R}\right)^2 + \omega_{s2}^2\left[-\ln\left(\frac{\gamma|q_z|\,R}{2}\right) + 0.6083\,\frac{\varepsilon_{s2}}{\varepsilon_{s1}}\right]\right\}^{1/2}. \tag{47}$$

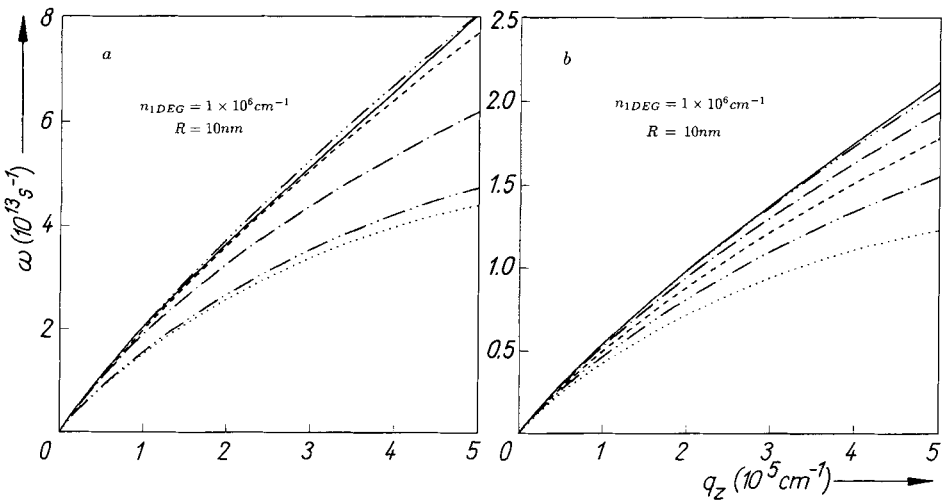

Fig. 3. Dispersion relation of the intrasubband plasmon of a) InSb–MOS and b) GaAs–AlAs CQWWs for different approximations for the case where one subband is occupied: ——— full RPA, —·— (40), ····· (42), —··— (44), — — — (46), —···— (47)

In Fig. 3 the dispersion curves of the intrasubband plasmons are plotted for the different approximations derived above. It is seen that the new long-wavelength approximation given in (46) gives very good results over a wide range of the wave vector $q_z \leqq k_F^{01}$ in comparison to the full RPA dispersion curve. For instance, for the InSb–MOS CQWW the deviation from the RPA is for $q_z = 5 \times 10^5\ \mathrm{cm}^{-1}$ 11% for (46) and only 0.01% for (47). However, the errors resulting if one uses (40), (42), and (44) are 23%, 46%, and 43%, respectively. The corresponding values for the GaAs–AlAs system are 16%, 2%, and 8.2%, 42% and 26%, respectively. Hence, (46) and (47) are very suitable and simple approximations for the dispersion curve of the intrasubband plasmon.

5.1.2 Intersubband plasmons

The dispersion relation of the intersubband plasmons of the two-subband model assuming the EQL is given by (37). In Fig. 4 the full RPA dispersion curves of the intersubband plasmon are plotted including the image potential (solid line) and neglecting the image contribution (dashed line). The shaded area in the ω–q_z plane is the region where the single-particle intersubband excitations exist. The dispersion curves of the intersubband plasmons start at $q_z = 0$ at a frequency above the subband separation frequency. This shift is caused by many-particle effects. The depolarization shift resulting from resonance screening is obtained within the RPA. There is still a further contribution, caused by exchange and correlation effects which is beyond the RPA. But for usual carrier densities this contribution is very small in comparison to the depolarization shift. From Fig. 4 it is seen that the depolarization shift increases with increasing image effects. This image force contribution to the depolarization shift is different from zero also for $q_z = 0$ and in a wide range of the wave vector. If one compares the depolarization shift of the intersubband plasmon in CQWWs with that in rectangular QWWs [29] one finds that the depolarization shift is approximately 1.4 times smaller in CQWWs. In the small wave-vector limit, i.e.

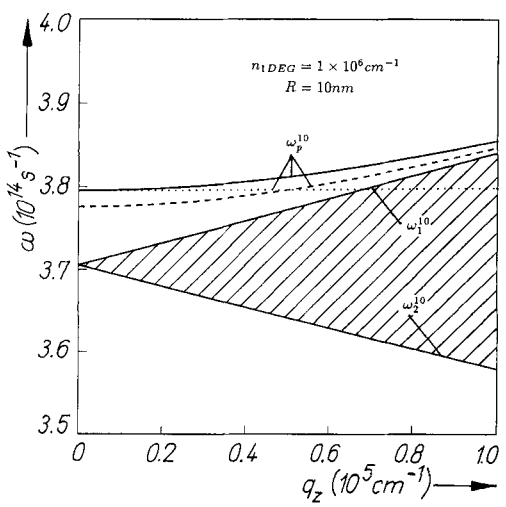

Fig. 4. Dispersion relation of the intersubband plasmon of a InSb–MOS CQWW where one subband is occupied. The dispersion curve calculated in RPA including image effects is given by a solid line and without image effects by a dashed line. The dispersion relation in the long-wavelength approximation of (49) is given by the dotted line. The shaded area corresponds to the single-particle intersubband continuum ($\mathrm{Im}\,\chi_{10}^{(1)}(q_z, \omega) \neq 0$) with the boundaries: $\omega_1^{10} = (\hbar k_F^{01}/m_e)\, q_z + (\hbar/2m_e)\, q_z^2 + \Omega_{10}$, $\omega_2^{10} = |-(\hbar k_F^{01}/m_e)\, q_z + (\hbar/2m_e)\, q_z^2 + \Omega_{10}|$

$v_F^{01} |q_z|, \hbar q_z^2/2m_e \ll \omega - \Omega_{10}$ it follows for the matrix polarization function

$$\chi_{10}^{(1)}(q_z, \omega) = \frac{n_{1\,\mathrm{DEG}}}{\pi\hbar} \frac{\Omega_{10}}{\omega^2 - \Omega_{10}^2} \left\{ 1 + \frac{\hbar q_z^2}{2m_e} \frac{\omega^2 + \Omega_{10}^2}{\Omega_{10}(\omega^2 - \Omega_{10}^2)} + O\left[\left(\frac{\hbar q_z}{m_e} \left(\frac{k_F^{01} + |q_z|/2}{\omega - \Omega_{10}} \right) \right)^2 \right] \right\}. \tag{48}$$

Using (48) in the dispersion relation (37), we obtain for the dispersion relation of the intersubband plasmon

$$\omega_p^{10} = \left\{ \Omega_{10}^2 + \frac{n_{1\,\mathrm{DEG}} e^2 f_{1010}^{C}(q_z)}{\pi\varepsilon_0\varepsilon_{s1}\hbar} \left[\Omega_{10} + \frac{\hbar q_z^2}{2m_e} + \sqrt{\left(\Omega_{10} + \frac{\hbar q_z^2}{2m_e} \right)^2 + \frac{4\pi\varepsilon_0\varepsilon_{s1}(\hbar\Omega_{10} q_z)^2}{n_{1\,\mathrm{DEG}} e^2 m_e f_{1010}^{C}(q_z)}} \right] \right\}^{1/2}. \tag{49}$$

The zero-order term of (49) reads

$$\omega_p^{10} = (1 + \alpha_{10})^{1/2} \Omega_{10}, \tag{50}$$

with

$$\alpha_{10} = \frac{n_{1\,\mathrm{DEG}} e^2}{\pi\varepsilon_0\varepsilon_{s1}\hbar\Omega_{10}} \left(\frac{2}{7} + \frac{1}{8} \frac{\varepsilon_{s1} - \varepsilon_{s2}}{\varepsilon_{s1} + \varepsilon_{s2}} \right). \tag{51}$$

This extra term in (51) is due to the depolarization effect. Hence, the explicit results, (50) and (51), show that for $\varepsilon_{s1} > \varepsilon_{s2}$ which is usually valid, the image forces increase the depolarization shift and the energy of a collective intersubband transition, as measured in FIR transmission experiments [6], also increases. From (50) and (51) it is explicitly seen that the image contribution is different from zero also for vanishing wave vectors. This is different from the case of intersubband plasmons in quasi-two-dimensional quantum wells where the image effects on the dispersion curves vanish for vanishing wave vector [46 to 48]. The contribution of the image effect to the depolarization shift is 22% for InSb–MOS and 4.8% for the GaAs–AlAs system.

We note that for the expansion of $\chi_{10}^{(1)}(q_z, \omega)$ given in (48) analogous problems, as for (39) in the case of the intrasubband plasmons, do not exist because the collective intersubband excitation has at $q_z = 0$ a finite depolarization shift.

It is interesting to compare our theoretical results with the experimental work of Merkt [6]. In these experiments the intersubband resonances in InSb–MOS and GaAs–$Ga_{1-x}Al_xAs$ QWWs were investigated. It was found that the depolarization shift ($q_z = 0$) for a InSb–MOS QWW with a wire width of 75 nm and $n_{1\,\mathrm{DEG}} = 1.5 \times 10^6\ \mathrm{cm}^{-1}$ is 8.4 meV and for a wire width of 85 nm and $n_{1\,\mathrm{DEG}} = 2.9 \times 10^6\ \mathrm{cm}^{-1}$ the depolarization shift is 11.5 meV. Using (51) of our theoretical model we obtain for the depolarization shift of the corresponding samples 8.77 and 10.8 meV, respectively. We note that this is an surprisingly good agreement (error only 4.4% and 6.1%). Hence, the experimental results could be explained by the image contribution.

Further in Fig. 4 the dispersion curve of the intersubband plasmon is plotted in the long-wavelength approximation of (49). The region for which the long-wavelength approximation describes well the full RPA dispersion curve is small because of the close boundary of the single-particle intersubband continuum.

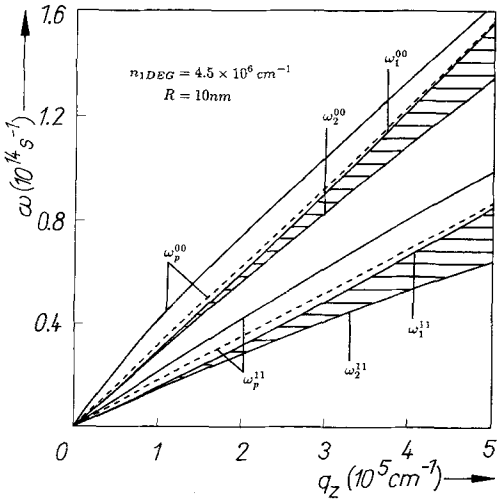

Fig. 5. Dispersion relation of the intrasubband plasmons of a InSb–MOS CQWW where two subbands are occupied. The dispersion curves calculated including image effects are given by the solid lines and without image effects by the dashed lines. The shaded areas correspond to the single-particle intrasubband continua ($\mathrm{Im}\,\chi_{00}^{(1)}(q_z, \omega) \neq 0$, $\mathrm{Im}\,\chi_{11}^{(1)}(q_z, \omega) \neq 0$) with the boundaries ω_1^{00}, ω_2^{00} and $\omega_1^{11} = (\hbar k_F^{11}/m_e)\,q_z + (\hbar/2m_e)\,q_z^2$, $\omega_2^{11} = |-(\hbar k_F^{11}/m_e)\,q_z + (\hbar/2m_e) \times q_z^2|$

5.2 *Two subbands are occupied*

5.2.1 *Intrasubband plasmons*

In the two-subband model assuming that two subbands are occupied, the matrix polarization function $\chi_{11}^{(1)}(q_z, \omega)$ is different from zero and hence, the dispersion relation describing the intrasubband modes with $n = 0$ is given by (36). In Fig. 5 the full RPA dispersion curves of the two-subband model with two populated subbands are plotted. In this case we have two intrasubband plasmon branches, ω_p^{00} and ω_p^{11} which are coupled modes. Hence, there exist also the two corresponding single-particle intrasubband continua. The small gap region between the boundaries ω_1^{11} and ω_2^{00} is free of Landau damping. Inside this region the intrasubband plasmon branch ω_p^{11} exists. We note that the additional intrasubband plasmon branch ω_p^{11} only occurs if more than one subband is occupied. To get deeper insight in the physical properties of both modes we derive analytical expressions. The use of the expansion for $P_{00}^{(1)}(q_z, \omega)$ in (39) and a similar one for $P_{11}^{(1)}(q_z, \omega)$ results in two dispersion curves. However, unfortunately the lower mode in lowest order of $|q_z|\,R$ has a frequency equal to zero and hence, the expansion in (39) for this mode is uncorrect. Following, we have to use for $P_{00}^{(1)}(q_z, \omega)$ the expansion of (45) and for $P_{11}^{(1)}(q_z, \omega)$ we use the expansion of (45) too, but replace k_F^{01} by k_F^{11}. Using these both expressions in the dispersion relation (36), we obtain in the lowest order of $|q_z|\,R$ two solutions,

$$\omega_p^{(00)}_{(11)} = |q_z|\,R \left\{ \frac{1}{2R^2}\left[(v_F^{01})^2 + (v_F^{11})^2\right] + \frac{1}{2}\,\omega_{s2}^2\left[-\ln\left(|q_z|\,R\right)\right] \right.$$
$$\pm \left[\frac{1}{4R^4}\left[(v_F^{01})^2 - (v_F^{11})^2\right]^2 + \frac{1}{2R^2}\,\omega_{s2}^2\left[-\ln\left(|q_z|\,R\right)\right] \frac{v_F^{01} - 2v_F^{11}}{v_F^{01} + 2v_F^{11}} \right.$$
$$\left. \left. \times (v_F^{01} - v_F^{11})^2 + \frac{1}{4}\,\omega_{s2}^4\left[\ln\left(|q_z|\,R\right)\right]^2 \right]^{1/2} \right\}^{1/2}. \tag{52}$$

For $q_z R \to 0$, (52) reads

$$\omega_p^{00} = \omega_{s2} |q_z| R[-\ln(|q_z| R)]^{1/2} \tag{53}$$

and

$$\omega_p^{11} = \left[v_F^{01} v_F^{11} \frac{2v_F^{01} + v_F^{11}}{2v_F^{11} + v_F^{01}} \right]^{1/2} |q_z| , \tag{54}$$

with $v_F^{11} = \hbar k_F^{11}/m_e$. The second branch, ω_p^{11}, has in lowest order of $|q_z| R$ a linear dispersion, depending only on the carrier density and not on the dielectric screening of the host and surrounding medium of the CQWW. However, we note that ω_p^{00} and ω_p^{11} are always coupled modes, even in the lowest order of $|q_z| R$, because ω_p^{00} depends on the electron concentration in both subbands and ω_p^{11} depends on the Fermi velocity of the lowest subband. As shown in [50] the upper mode, ω_p^{00}, behaves like an optical plasmon because the electron densities, induced in the upper and lower subbands oscillate in phase. For the lower mode, ω_p^{11}, the electron densities, induced in both subbands oscillate in anti-phase and hence, the mode ω_p^{11} is an acoustic plasmon.

In Fig. 5 the full RPA dispersion curves of the intrasubband plasmons including the image potential (solid lines) and neglecting the image contribution (dashed lines) are plotted. In this figure we denote the two roots of the full RPA dispersion curves as ω_p^{00} and ω_p^{11}. It is seen that the image effects influence the (0–0) branch at small wave vectors more than the (1–1) branch. For small wave vectors the image effects vanish for the (1–1) branch, explicitly seen from the analytical result of (54).

In Fig. 6 the dispersion curves of the intrasubband plasmons are plotted for the different approximations derived above. It is seen that the long-wavelength approximation given in (52) gives very good results in the whole plotted range

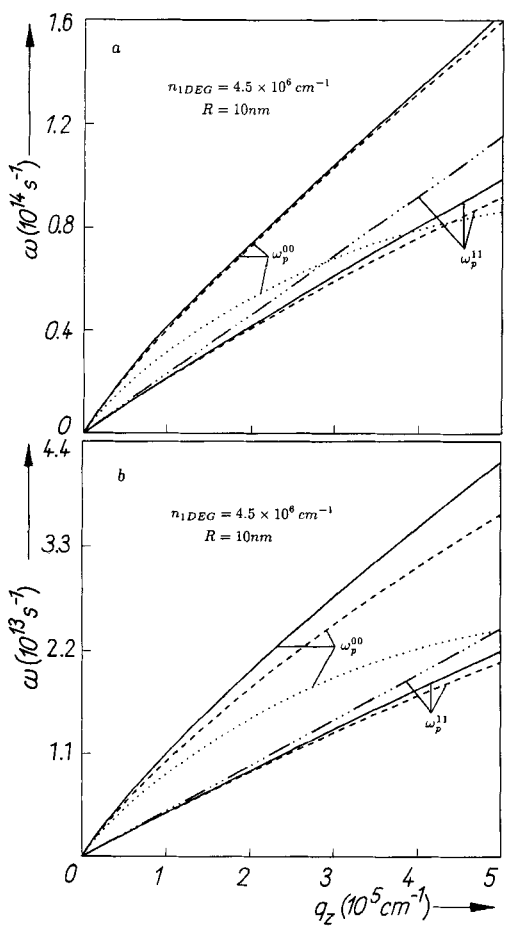

Fig. 6. Dispersion relation of the intrasubband plasmons of a) InSb–MOS and b) GaAs–AlAs CQWW for the case where two subbands are occupied. The dispersion curves calculated including image effects within the RPA are given by solid lines and of the long-wavelength approximations are given by — — — (52), · · · · · · · (53), — ·· — (54)

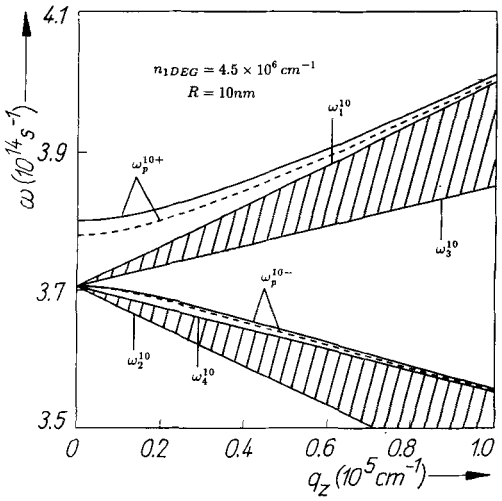

Fig. 7. Dispersion relation of the intersubband plasmons of a InSb–MOS CQWW where two subbands are occupied. The dispersion curves calculated including image effects within the RPA are given by the solid lines and without image effects by the dashed lines. The shaded area corresponds to the single-particle intersubband continuum (Im $\chi_{10}^{(1)}(q_z, \omega) \neq 0$) with the boundaries ω_1^{10}, ω_2^{10} and $\omega_3^{10} = |(\hbar k_F^{11}/m_e)\, q_z - (\hbar/2m_e)\, q_z^2 + \Omega_{10}|$, $\omega_4^{10} = |-(\hbar k_F^{11}/m_e)\, q_z - (\hbar/2m_e)\, q_z^2 + \Omega_{10}|$

of the wave vector in comparison to the full RPA dispersion curves. For instance, for the InSb–MOS CQWW the deviation from the RPA is 2% for the upper branch and 7% for the lower branch at $q_z = 5 \times 10^5\ \mathrm{cm}^{-1}$. For the GaAs–AlAs system the deviation from the RPA for the upper mode, ω_p^{00}, is 11% and 5% for the lower mode ω_p^{11}. Whereas (54) is a good approximation of the mode ω_p^{11}, (53) is only a good approximation of the mode ω_p^{00} for very small wave vectors and electron densities.

5.2.2 *Intersubband plasmons*

The dispersion relation of the intersubband plasmons of the two-subband model assuming that two subbands are occupied is given by (37). In Fig. 7 the full RPA dispersion curves of the intersubband plasmons are plotted including the image potential (solid lines) and neglecting the image contribution (dashed lines). The shaded area in the ω–q_z plane is the single-particle intersubband continuum. If two subbands are occupied, a gap region, the area between the curves ω_3^{10} and ω_4^{10}, arises, for which Im $\chi_{10}^{(1)}(q_z, \omega) = 0$. Within this region an additional intersubband plasmon mode, ω_p^{10-}, exists. Firstly, this additional branch of intersubband plasmons was predicted by Wendler et al. [29] and Mendoza and Schaich [34]. It is seen from Fig. 7 that the fundamental mode, ω_p^{10+}, has a finite depolarization shift and a positive dispersion, the additional mode, ω_p^{10-}, has a vanishing depolarization shift ($q_z = 0$) and a negative dispersion. In a recent resonant inelastic light scattering experiment, Goñi et al. [9] used a QWW with two occupied subbands. In the gap region of the single-particle intersubband continuum they observed an intersubband excitation which we identify with the here obtained mode ω_p^{10-}. If one compares Fig. 4 and 7 it is evident that the depolarization shift of ω_p^{10+} decreases if the electron density increases in the case that the second subband is just occupied. This effect is physically well understood [30]. For vanishing wave vector the intersubband resonance frequency of the fundamental mode is given by (50) $\omega_p^{10+} = (1 + \alpha_{10+})^{1/2}\, \Omega_{10}$, where α_{10+} is given by (51) if one replaces $n_{1\,\mathrm{DEG}}$ by $(n_{1\,\mathrm{DEG}}^{01} - n_{1\,\mathrm{DEG}}^{11})$. The densities $n_{1\,\mathrm{DEG}}^{ml}$ of each subband are given by (7) in the form $n_{1\,\mathrm{DEG}} = \sum_m \sum_l n_{1\,\mathrm{DEG}}^{ml}$. Further, it can be seen that the influence of the image forces is smaller

in the case of two occupied subbands (Fig. 7) than in the case of one occupied subband (Fig. 4). To get a deeper insight in the physical properties of the additional mode we want to derive an analytical expression in the long-wavelength approximation. Assuming a dispersion relation of the form

$$\omega_{\mathrm{p}}^{10-} \approx \Omega_{10} - \xi q_z^2 , \tag{55}$$

from (25) follows

$$P_{01}^{(1)}(q_z, \omega) \approx -\frac{1}{2\pi^2 \hbar \Omega_{10}} (k_{\mathrm{F}}^{01} - k_{\mathrm{F}}^{11}) \tag{56}$$

and

$$P_{10}^{(1)}(q_z, \omega) \approx -\frac{m_{\mathrm{e}}}{2\pi^2 \hbar^2} \left[\frac{1}{k_{\mathrm{F}}^{01}} + \frac{1}{k_{\mathrm{F}}^{11}} - \frac{2m_{\mathrm{e}}\xi}{\hbar} \left(\frac{1}{k_{\mathrm{F}}^{11}} - \frac{1}{k_{\mathrm{F}}^{01}} \right) \right]. \tag{57}$$

Using (56) and (57) in (37) we obtain

$$\xi = \frac{\pi^2 \hbar^2}{m_{\mathrm{e}} V_{1010}^{\mathrm{s}}(0)} \frac{v_{\mathrm{F}}^{01} v_{\mathrm{F}}^{11}}{v_{\mathrm{F}}^{01} - v_{\mathrm{F}}^{11}} + \frac{\hbar}{2m_{\mathrm{e}}} \frac{v_{\mathrm{F}}^{01} + v_{\mathrm{F}}^{11}}{v_{\mathrm{F}}^{01} - v_{\mathrm{F}}^{11}} + \frac{v_{\mathrm{F}}^{01} v_{\mathrm{F}}^{11}}{2\Omega_{10}} . \tag{58}$$

Because of $v_F^{01} > v_{\mathrm{F}}^{11}$ it follows that for all electron densities $\xi > 0$ is valid. Hence, the explicit analytical expression of $\omega_{\mathrm{p}}^{10-}$, (55), shows negative dispersion.

6. Electric Dipole Moment of the Collective Excitations

In previous sections, we have calculated the collective excitation frequencies of a CQWW. The calculated dispersion curves correspond to the positions of minima in FIR transmission experiments if the applied light couples with the modes. In this chapter we calculate the electric dipole moment of the modes. If this is different from zero the corresponding plasmon can be excited in FIR experiments if a grating-coupler is used to match the wave vectors of the incident light and plasmons. The induced electric dipole moment is defined by

$$\boldsymbol{p}_{\mathrm{ind}}(\omega) = -e \int \mathrm{d}^3 x \, \boldsymbol{x} \, n_{\mathrm{ind}}(\boldsymbol{x}, \omega) . \tag{59}$$

Because of the neutrality of the sample the total induced electron number density is zero and hence, the electric dipole moment is independent of the choice of the coordinate system. The induced electron number density is given by (12). This equation can be expressed in the form

$$\begin{aligned} n_{\mathrm{ind}}(\boldsymbol{x}, \omega) &= \sum_{n=-\infty}^{\infty} \sum_{q_z=-\infty}^{\infty} n_{\mathrm{ind}}^{(n)}(\boldsymbol{x}; q_z \mid \omega) \\ &= \frac{1}{2\pi L_z} \sum_{n=-\infty}^{\infty} \sum_{q_z=-\infty}^{\infty} \mathrm{e}^{in\varphi} \, \mathrm{e}^{iq_z z} \, n_{\mathrm{ind}}^{(n)}(r; q_z, \omega) , \end{aligned} \tag{60}$$

with

$$n_{\mathrm{ind}}^{(n)}(r; q_z \mid \omega) = \sum_{m \geqq -[n/2]}^{\infty} \sum_{l,l'=1}^{\infty} \eta_{\substack{m+n\,m \\ l\quad l'}}(r) \, \chi^{(1)}_{\substack{m+n\,m \\ l\quad l'}}(q_z, \omega) \, V^{\mathrm{sc}}_{\substack{m+n\,m \\ l\quad l'}}(q_z, \omega) . \tag{61}$$

Here $V^{sc}_{\substack{m+n\,m\\ l\;\;l'}}(q_z, \omega)$ is given by (30). According to the cylindrical symmetry of the problem the dipole moments for different quantum numbers n are decoupled. Hence, the induced electric dipole moment of the plasmon modes with equal $n = \Delta m$, $\boldsymbol{p}^{(n)}_{ind}(q_z, \omega)$ is given by

$$\boldsymbol{p}^{(n)}_{ind}(q_z, \omega) = -e \int_0^R \mathrm{d}r\, r \int_0^{2\pi} \mathrm{d}\varphi \int_0^{L_z} \mathrm{d}z\, \boldsymbol{x} n^{(n)}_{ind}(\boldsymbol{x}; q_z \mid \omega)\,. \tag{62}$$

Now it is possible to calculate $\boldsymbol{p}^{(n)}_{ind}(q_z, \omega)$ using the RPA expression of $n^{(n)}_{ind}(\boldsymbol{x}; q_z \mid \omega)$ for the general case of N subbands from which M are occupied. Further, we perform the integrals using the correct wave functions of (5). In the case of the intrasubband modes ($n = 0$) we obtain for the components of $\boldsymbol{p}^{(n)}_{ind}(q_z, \omega) = (p^{(n)}_x(q_z, \omega), p^{(n)}_y(q_z, \omega), p^{(n)}_z(q_z, \omega))$, that $p^{(0)}_x(q_z, \omega) = p^{(0)}_y(q_z, \omega) = 0$ and $p^{(0)}_z(q_z, \omega) \neq 0$. Hence, intrasubband plasmon can be excited in FIR transmission if the light is polarized along the wire axis.

For the intersubband plasmons ($n \neq 0$) we obtain for $n \neq \pm 1$ a vanishing induced electric dipole moment: $p^{(n)}_x(q_z, \omega) = p^{(n)}_y(q_z, \omega) = p^{(n)}_z(q_z, \omega) = 0$. Hence, all intersubband plasmon branches $\omega_{p\;\substack{m+n\,m\\ l\;\;l'}}$ with $n \neq \pm 1$ have vanishing electric dipole moments and therefore cannot be excited in a FIR experiment. The induced electric dipole moments also vanish in the case $n = \pm 1$ if $q_z \neq 0$. In the case $n = \pm 1$ but if $q_z = 0$ we obtain: $p^{(n)}_x(q_z, \omega) \neq 0$, $p^{(n)}_y(q_z, \omega) \neq 0$, and $p^{(n)}_z(q_z, \omega) = 0$. Hence, in the CQWW it is impossible to excite intersubband plasmons with finite wave vector ($q_z \neq 0$) using FIR transmission spectroscopy. One only can obtain collective intersubband resonances ($q_z = 0$) for $n = \pm 1$. The obtained dipole selection rules are independent of l and l'. Hence, if a transition is dipole-allowed according to $n(\Delta m)$ this is possible for all Δl.

7. Conclusion

In this paper we have studied in great detail the collective excitations of cylindrical quantum-well wires. For a two-subband model we have calculated the full RPA dispersion curves of the intra- and intersubband plasmons for one and two occupied subbands including image effects. We have derived analytical expressions for the Coulomb interaction potential. We have shown the importance of the inclusion of the image effects on the Coulomb interaction potential in a relatively wide range of the wave vector ($|q_z| R \leqq 1$). In general, the image potential increases the frequencies of the intra- and intersubband plasmons for GaAs–AlAs and InSb–MOS systems. The influence of the image forces is stronger for the intrasubband plasmons than for the intersubband plasmons. For the GaAs–AlAs QWW the image forces have only a very small influence on the dispersion curves of the Q1D plasmons. Further, we have derived new analytic expressions for the dispersion curves of the intra- and intersubband plasmons, valid in a wide range wave vectors, up to $q_z \leqq k^{01}_F$ for intrasubband plasmons and up to $q_z \approx 10^5\ \mathrm{cm}^{-1}$ for intersubband plasmons. These expressions are suitable to explain some of the obtained experimental results on intra- and intersubband plasmons. Using the analytical expression for the intersubband plasmons we can show that the experimental data of Merkt [6] are very well explained by image effects. In the case of two occupied subbands there exist two intrasubband and two intersubband plasmon branches. The higher frequency intrasubband branch behaves like an optical plasmon and the other three branches like a acoustic plasmons [50]. Also in this case we have derived suitable long-wavelength approximations of the dispersion relation. The lower intrasubband plasmon mode, connected with the second occupied subband is independent

of the dielectric screening and shows for small wave vectors a linear dispersion in difference to the upper mode which shows a logarithmic dispersion. The upper intersubband plasmon branch has a finite depolarization shift and a positive dispersion, but the additional lower intersubband plasmon branch has a zero depolarization shift and a negative dispersion.

We have shown that intrasubband plasmons can interact with light polarized along the wire axis and only intersubband resonances ($q_z = 0$) for $n = \pm 1$ can be observed in FIR experiments, if the light is polarized perpendicular to the wire axis.

Acknowledgement

We gratefully acknowledge financial support by the Deutsche Forschungsgemeinschaft (DFG), project We 1532/3-1.

Appendix A

Green's function

In this Appendix we evaluate the electrostatic Green's function of Poisson's equation for the CQWW. This function is defined by

$$\nabla \cdot (\varepsilon_s(x_\perp) \nabla D(x, x')) = -\delta(x - x'), \tag{A1}$$

where according to symmetry

$$D(x, x') = \frac{1}{2\pi L_z} \sum_{n=-\infty}^{\infty} \sum_{q_z=-\infty}^{\infty} e^{in(\varphi - \varphi')} e^{iq_z(z-z')} D_n(r, r'; q_z) \tag{A2}$$

is valid. Using (A2) in (A1) it follows:

$$\left\{\frac{1}{r}\frac{d}{dr}\left[\varepsilon_s(r)\, r \frac{d}{dr}\right] - \varepsilon_s(r)\left(\frac{n^2}{r^2} + q_z^2\right)\right\} D_n(r, r'; q_z) = -\frac{1}{r}\delta(r - r'), \tag{A3}$$

where $D_n(r, r'; q_z)$ is the radial Green's function. To solve (A3) we need a special solution $D_n^{\mathrm{dir}}(r, r'; q_z)$ of the inhomogeneous and a general solution $D_n^{\mathrm{im}}(r, r'; q_z)$ of the homogeneous equation. The sum of both must fulfil the boundary conditions. We require continuity of $D_n(r, r'; q_z)$ and of $\varepsilon_{sv}\, \partial/\partial r\, (D_n(r, r'; q_z))$ at the cylinder interface at $r = R$ and vanishing $D_n(r, r'; q_z)$ at $r = \infty$. The special solution of (A3) is

$$D_n^{\mathrm{dir}}(r, r'; q_z) = \frac{1}{\varepsilon_{s1}} \mathrm{I}_n(|q_z|\, r_<)\, \mathrm{K}_n(|q_z|\, r_>), \tag{A4}$$

where $\mathrm{I}_n(x)$ and $\mathrm{K}_n(x)$ are modified Bessel functions and $\varepsilon_s(r) = \varepsilon_{s1}$ for $r \leqq R$ and $\varepsilon_s(r) = \varepsilon_{s2}$ for $r > R$. Further $r_< = \min(r, r')$ and $r_> = \max(r, r')$ is valid. For a general solution of (A3), $D_n(r, r'; q_z) = D_n^{\mathrm{dir}}(r, r'; q_z) + D_n^{\mathrm{im}}(r, r'; q_z)$ we make the ansatz

$$D_n(r, r'; q_z) = \begin{cases} B_n \mathrm{I}_n(|q_z|\, r) + \varepsilon_{s1}^{-1} \mathrm{I}_n(|q_z|\, r_<)\, \mathrm{K}_n(|q_z|\, r_>) & \text{if } r \leqq R, \\ A_n \mathrm{K}_n(|q_z|\, r); & \text{if } r > R. \end{cases} \tag{A5}$$

Using the boundary conditions for the radial Green's functions (A5) we obtain

$$A_n = \frac{\mathrm{I}_n(|q_z|\, r')}{|q_z|\, R[\varepsilon_{s1} \mathrm{I}_n'(|q_z|\, R)\, \mathrm{K}_n(|q_z|\, R) - \varepsilon_{s2} \mathrm{I}_n(|q_z|\, R)\, \mathrm{K}_n'(|q_z|\, R)]} \tag{A6}$$

and

$$B_n = \frac{(\varepsilon_{s1} - \varepsilon_{s2})\, I_n(|q_z| r')\, K_n(|q_z| R)\, K_n'(|q_z| R)}{\varepsilon_{s1}[\varepsilon_{s2} I_n(|q_z| R)\, K_n'(|q_z| R) - \varepsilon_{s1} I_n'(|q_z| R)\, K_n(|q_z| R)]}, \tag{A7}$$

with $I_n'(x)$ and $K_n'(x)$ the derivatives of $I_n(x)$ and $K_n(x)$ at x, respectively.

We notice that the radial Green's function is related to the radial part of the Coulomb potential by

$$V_n^s(r, r'; q_z) = \frac{e^2}{\varepsilon_0}[D_n^{dir}(r, r'; q_z) + D_n^{im}(r, r'; q_z)]. \tag{A8}$$

The first term represents the direct Coulomb potential whereas the second term represents the image potential. The form factors are defined by

$$V^s_{\substack{m_1 m_2 m_3 m_4 \\ l_1 l_2 l_3 l_4}}(q_z) = \frac{e^2}{\varepsilon_0 \varepsilon_{s1}} f^C_{\substack{m_1 m_2 m_3 m_4 \\ l_1 l_2 l_3 l_4}}(q_z)\, \delta_{m_2 m_1 - n} \delta_{m_4 m_3 + n}, \tag{A9}$$

with

$$f^C_{\substack{m_1 m_2 m_3 m_4 \\ l_1 l_2 l_3 l_4}}(q_z) = f^{dir}_{\substack{m_1 m_2 m_3 m_4 \\ l_1 l_2 l_3 l_4}}(q_z) + f^{im}_{\substack{m_1 m_2 m_3 m_4 \\ l_1 l_2 l_3 l_4}}(q_z) \tag{A10}$$

and

$$f^{dir}_{\substack{m_1 m_1 - n m_3 m_3 + n \\ l_1 l_3 l_3 l_4}}(q_z) = \varepsilon_{s1} \int dr\, r \int dr'\, r' \eta^*_{\substack{m_1 m_1 - n \\ l_1 l_2}}(r)\, D_n^{dir}(r, r'; q_z)\, \eta^*_{\substack{m_3 m_3 + n \\ l_3 l_3}}(r'), \tag{A11}$$

$$f^{im}_{\substack{m_1 m_1 - n m_3 m_3 + n \\ l_1 l_2 l_3 l_4}}(q_z) = \varepsilon_{s1} \int dr\, r \int dr'\, r' \eta^*_{\substack{m_1 m_1 - n \\ l_1 l_2}}(r)\, D_n^{im}(r, r'; q_z)\, \eta^*_{\substack{m_3 m_3 + n \\ l_3 l_3}}(r'). \tag{A12}$$

Appendix B

Matrix elements of the Coulomb potential

In this Appendix we calculate the matrix elements of the direct Coulomb potential and the image potential defined in (33) to (35) using the wave functions of (8), (9) and the Green's function calculated in Appendix A (A5) to (A7). Because for the two lowest subbands $l_1 = l_2 = l_3 = l_4 = 1$ is valid, we omit these quantum numbers in the following. The calculation is straightforward with the following results:

$$V^{dir}_{0000}(q_z) = \frac{36e^2}{\varepsilon_0 \varepsilon_{s1}(q_z R)^2}\left\{\frac{1}{10} - \frac{2}{3(q_z R)^2} + \frac{32}{3(q_z R)^4} - \frac{64}{(q_z R)^4} I_3(|q_z| R)\, K_3(|q_z| R)\right\}, \tag{B1}$$

$$V^{im}_{0000}(q_z) = \frac{36e^2}{\varepsilon_0 \varepsilon_{s1}(q_z R)^2} \left\{\frac{64(\varepsilon_{s1} - \varepsilon_{s2})\, I_3^2(|q_z| R)\, K_0(|q_z| R)\, K_1(|q_z| R)}{(q_z R)^4 [\varepsilon_{s1} I_1(|q_z| R)\, K_0(|q_z| R) + \varepsilon_{s2} I_0(|q_z| R)\, K_1(|q_z| R)]}\right\}, \tag{B2}$$

$$V^{dir}_{1100}(q_z) = \frac{144e^2}{\varepsilon_0 \varepsilon_{s1}(q_z R)^2}\left\{\frac{1}{60} - \frac{1}{15(q_z R)^2} + \frac{8}{3(q_z R)^4} - \frac{64}{(q_z R)^4} K_3(|q_z| R) \times \left[I_3(|q_z| R) - \frac{6}{|q_z| R} I_4(|q_z| R)\right]\right\}, \tag{B3}$$

$$V^{\mathrm{im}}_{1100}(q_z) = \frac{144e^2}{\varepsilon_0\varepsilon_{s1}(q_zR)^2}\left\{64(\varepsilon_{s1}-\varepsilon_{s2})\,\mathrm{I}_3(|q_z|R)\left[\mathrm{I}_3(|q_z|R)-\frac{6}{|q_z|R}\,\mathrm{I}_4(|q_z|R)\right]\right.$$
$$\left.\times\frac{\mathrm{K}_0(|q_z|R)\,\mathrm{K}_1(|q_z|R)}{(q_zR)^4\,[\varepsilon_{s1}\mathrm{I}_1(|q_z|R)\,\mathrm{K}_0(|q_z|R)+\varepsilon_{s2}\mathrm{I}_0(|q_z|R)\,\mathrm{K}_1(|q_z|R)]}\right\}, \tag{B4}$$

$$V^{\mathrm{dir}}_{1111}(q_z) = \frac{576e^2}{\varepsilon_0\varepsilon_{s1}(q_zR)^2}\left\{\frac{1}{210}-\frac{1}{15(q_zR)^2}+\frac{64}{15(q_zR)^4}+\frac{96}{(q_zR)^6}-\frac{64}{(q_zR)^4}\right.$$
$$\left.\times\left[\mathrm{I}_3(|q_z|R)-\frac{6}{|q_z|R}\,\mathrm{I}_4(|q_z|R)\right]\left[\mathrm{K}_3(|q_z|R)+\frac{6}{|q_z|R}\,\mathrm{K}_4(|q_z|R)\right]\right\}, \tag{B5}$$

$$V^{\mathrm{im}}_{1111}(q_z) = \frac{576e^2}{\varepsilon_0\varepsilon_{s1}(q_zR)^2}\left\{64(\varepsilon_{s1}-\varepsilon_{s2})\left[\mathrm{I}_3(|q_z|R)-\frac{6}{|q_z|R}\,\mathrm{I}_4(|q_z|R)\right]^2\right.$$
$$\left.\times\frac{\mathrm{K}_0(|q_z|R)\,\mathrm{K}_1(|q_z|R)}{(q_zR)^4\,[\varepsilon_{s1}\mathrm{I}_1(|q_z|R)\,\mathrm{K}_0(|q_z|R)+\varepsilon_{s2}\mathrm{I}_0(|q_z|R)\,\mathrm{K}_1(|q_z|R)]}\right\}, \tag{B6}$$

$$V^{\mathrm{dir}}_{1010}(q_z) = \frac{144e^2}{\varepsilon_0\varepsilon_{s1}(q_zR)^2}\left\{\frac{1}{60}-\frac{4}{15(q_zR)^2}+\frac{8}{(q_zR)^4}\right.$$
$$\left.-\frac{64}{(q_zR)^4}\,\mathrm{I}_4(|q_z|R)\,\mathrm{K}_4(|q_z|R)\right\}, \tag{B7}$$

$$V^{\mathrm{im}}_{1010}(q_z) = \frac{144e^2}{\varepsilon_0\varepsilon_{s1}(q_zR)^2}$$
$$\times\left\{\frac{64(\varepsilon_{s1}-\varepsilon_{s2})\,\mathrm{I}_4^2(|q_z|R)\,\mathrm{K}_1(|q_z|R)\,\mathrm{K}_1'(|q_z|R)}{(q_zR)^4\,[\varepsilon_{s2}\mathrm{I}_1(|q_z|R)\,\mathrm{K}_1'(|q_z|R)-\varepsilon_{s1}\mathrm{I}_1'(|q_z|R)\,\mathrm{K}_1(|q_z|R)]}\right\}. \tag{B8}$$

Here $\mathrm{I}_m(x)$ and $\mathrm{K}_m(x)$ are modified Bessel functions and $\mathrm{I}_m'(x)$ and $\mathrm{K}_m'(x)$ their derivatives.

Because the matrix elements always contain the product $|q_z|R$, the limit of a large (small) wave vector is the same as a large (small) radius of the CQWW. Using the well-known asymptotic expressions for the modified Bessel functions, we obtain for $|q_z|R \ll 1$

$$V^{\mathrm{dir}}_{0000}(q_z) \approx -\frac{e^2}{\varepsilon_0\varepsilon_{s1}}\left\{\ln\left(\frac{\gamma|q_z|R}{2}\right)-0.6083\right.$$
$$\left.+(q_zR)^2\left[\frac{1}{8}\ln\left(\frac{\gamma|q_z|R}{2}\right)-0.1450\right]\right\}, \tag{B9}$$

$$V^{\mathrm{im}}_{0000}(q_z) \approx \frac{e^2}{\varepsilon_0}\left(\frac{1}{\varepsilon_{s1}}-\frac{1}{\varepsilon_{s2}}\right)\left\{\ln\left(\frac{\gamma|q_z|R}{2}\right)\right.$$
$$\left.+(q_zR)^2\left[\frac{\varepsilon_{s1}}{2\varepsilon_{s2}}\ln^2\left(\frac{\gamma|q_z|R}{2}\right)+\frac{1}{4}\ln\left(\frac{\gamma|q_z|R}{2}\right)-\frac{1}{4}\right]\right\}, \tag{B10}$$

$$V^{\mathrm{dir}}_{1100}(q_z) \approx -\frac{e^2}{\varepsilon_0\varepsilon_{s1}}\left\{\ln\left(\frac{\gamma\,|q_z|\,R}{2}\right) - 0.4476 + (q_zR)^2\left[\frac{13}{80}\ln\left(\frac{\gamma\,|q_z|\,R}{2}\right) - 0.1715\right]\right\}, \tag{B11}$$

$$V^{\mathrm{im}}_{1100}(q_z) \approx \frac{e^2}{\varepsilon_0}\left(\frac{1}{\varepsilon_{s1}} - \frac{1}{\varepsilon_{s2}}\right)\left\{\ln\left(\frac{\gamma\,|q_z|\,R}{2}\right) + (q_zR)^2\left[\frac{\varepsilon_{s1}}{2\varepsilon_{s2}}\ln^2\left(\frac{\gamma\,|q_z|\,R}{2}\right) + \frac{13}{80}\ln\left(\frac{\gamma\,|q_z|\,R}{2}\right) - \frac{1}{4}\right]\right\}, \tag{B12}$$

$$V^{\mathrm{dir}}_{1111}(q_z) \approx -\frac{e^2}{\varepsilon_0\varepsilon_{s1}}\left\{\ln\left(\frac{\gamma\,|q_z|\,R}{2}\right) - 0.3673 + (q_zR)^2\left[\frac{1}{5}\ln\left(\frac{\gamma\,|q_z|\,R}{2}\right) - 0.0735\right]\right\}, \tag{B13}$$

$$V^{\mathrm{im}}_{1111}(q_z) \approx \frac{e^2}{\varepsilon_0}\left(\frac{1}{\varepsilon_{s1}} - \frac{1}{\varepsilon_{s2}}\right)\left\{\ln\left(\frac{\gamma\,|q_z|\,R}{2}\right) + (q_zR)^2\left[\frac{\varepsilon_{s1}}{2\varepsilon_{s2}}\ln^2\left(\frac{\gamma\,|q_z|\,R}{2}\right) + \frac{1}{5}\ln\left(\frac{\gamma\,|q_z|\,R}{2}\right) - \frac{1}{4}\right]\right\}, \tag{B14}$$

$$V^{\mathrm{dir}}_{1010}(q_z) \approx \frac{e^2}{\varepsilon_0\varepsilon_{s1}}\left\{\frac{2}{7} + (q_zR)^2\left[\frac{1}{16}\ln\left(\frac{\gamma\,|q_z|\,R}{2}\right) - 0.0453\right]\right\}, \tag{B15}$$

$$V^{\mathrm{im}}_{1010}(q_z) \approx \frac{e^2}{\varepsilon_0\varepsilon_{s1}}\,\frac{\varepsilon_{s1} - \varepsilon_{s2}}{\varepsilon_{s1} + \varepsilon_{s2}} \times\left\{\frac{1}{8} + \frac{(q_zR)^2}{4}\left[\frac{1}{16}\,\frac{\varepsilon_{s2} - \varepsilon_{s1}}{\varepsilon_{s2} + \varepsilon_{s1}}\left(1 + 4\ln\left(\frac{\gamma\,|q_z|\,R}{2}\right)\right) - \frac{1}{5}\right]\right\}, \tag{B16}$$

where $\gamma = 1.781072418$ is the Euler constant.

In the opposite limit, i.e. $|q_z|\,R \gg 1$ the expressions for the Coulomb potential matrix elements are obtained to be

$$V^{\mathrm{dir}}_{0000}(q_z) \approx \frac{3.6e^2}{\varepsilon_0\varepsilon_{s1}(q_zR)^2}, \tag{B17}$$

$$V^{\mathrm{im}}_{0000}(q_z) \approx \frac{1152e^2}{\varepsilon_0\varepsilon_{s1}(q_zR)^7}\,\frac{\varepsilon_{s1} - \varepsilon_{s2}}{\varepsilon_{s1} + \varepsilon_{s1}}, \tag{B18}$$

$$V^{\mathrm{dir}}_{1100}(q_z) \approx \frac{2.4e^2}{\varepsilon_0\varepsilon_{s1}(q_zR)^2}, \tag{B19}$$

$$V^{\mathrm{im}}_{1100}(q_z) \approx \frac{4608e^2}{\varepsilon_0\varepsilon_{s1}(q_zR)^7}\,\frac{\varepsilon_{s1} - \varepsilon_{s2}}{\varepsilon_{s1} + \varepsilon_{s1}}, \tag{B20}$$

$$V^{\mathrm{dir}}_{1111}(q_z) \approx \frac{2.743e^2}{\varepsilon_0\varepsilon_{s1}(q_zR)^2}, \tag{B21}$$

$$V^{\mathrm{im}}_{1111}(q_z) \approx \frac{18432e^2}{\varepsilon_0\varepsilon_{s1}(q_zR)^7}\,\frac{\varepsilon_{s1}-\varepsilon_{s2}}{\varepsilon_{s1}+\varepsilon_{s1}}, \tag{B22}$$

$$V^{\mathrm{dir}}_{1010}(q_z) \approx \frac{2.4e^2}{\varepsilon_0\varepsilon_{s1}(q_zR)^2}, \tag{B23}$$

$$V^{\mathrm{im}}_{1010}(q_z) \approx \frac{4608e^2}{\varepsilon_0\varepsilon_{s1}(q_zR)^7}\,\frac{\varepsilon_{s1}-\varepsilon_{s2}}{\varepsilon_{s1}+\varepsilon_{s1}}. \tag{B24}$$

Hence, in this limit image effects become unimportant. For a large radius of the CQWW the field lines are mostly inside of the wire with ε_{s1} and, hence, the surrounding medium has nearly no influence on the Coulomb interaction.

References

[1] B. J. VAN WEES, H. VAN HOUTEN, C. W. J. BEENAKKER, J. G. WILLIAMSON, L. P. KOUWENHOVEN, D. VAN DER MAREL, and C. T. FOXON, Phys. Rev. Letters **60**, 848 (1988).
[2] D. A. WHARAM, T. J. THORNTON, R. NEWBURY, M. PEPPER, H. AHMED, J. E. F. FROST, D. G. HASKO, D. C. PEACOCK, D. A. RITCHIE, and G. A. C. JONES, J. Phys. C **21**, L209 (1988).
[3] W. HANSEN, M. HORST, J. P. KOTTHAUS, U. MERKT, CH. SIKORSKI, and K. PLOOG, Phys. Rev. Letters **58**, 2586 (1987).
[4] F. BRINKOP, W. HANSEN, J. P. KOTTHAUS, and K. PLOOG, Phys. Rev. B **37**, 6547 (1988).
[5] T. DEMEL, D. HEITMANN, P. GRAMBOW, and K. PLOOG, Phys. Rev. B **38**, 12372 (1988).
[6] U. MERKT, Superlattices and Microstructures **6**, 341 (1989).
[7] T. DEMEL, D. HEITMANN, P. GRAMBOW, and K. PLOOG, Phys. Rev. Letters **66**, 2657 (1991).
[8] H. DREXLER, W. HANSEN, J. P. KOTTHAUS, M. HOLLAND, and S. P. BEAUMONT, Phys. Rev. B **46**, 12849 (1992).
[9] A. R. GOÑI, A. PINCZUK, J. S. WEINER, J. M. CALLEJA, B. S. DENNIS, L. N. PFEIFFER, and K. W. WEST, Phys. Rev. Letters **67**, 3298 (1991).
[10] A. R. GOÑI, A. PINCZUK, J. S. WEINER, B. S. DENNIS, L. N. PFEIFFER, and K. W. WEST, Phys. Rev. Letters **70**, 1151 (1993).
[11] A. SCHMELLER, A. R. GOÑI, A. PINCZUK, J. S. WEINER, J. M. CALLEJA, B. S. DENNIS, L. N. PFEIFFER, and K. W. WEST, in: Proc. 6th Internat. Conf. Modulated Semiconductor Structures, Garmisch-Partenkirchen (Germany) 1993 (p. 1022).
[12] S. DAS SARMA and W. Y. LAI, Phys. Rev. B **32**, 1401 (1985).
[13] W. QUE and G. KIRCZENOW, Phys. Rev. B **37**, 7153 (1988).
[14] W. QUE and G. KIRCZENOW, Phys. Rev. B **39**, 5998 (1989).
[15] Q. LI and S. DAS SARMA, Phys. Rev. B **40**, 5860 (1989).
[16] A. V. CHAPLIK, Superlattices and Microstructures **6**, 329 (1989).
[17] HAO CHEN, YUN ZHU, and SHIXUN ZHOU, Phys. Rev. B **36**, 8189 (1987).
[18] YUN ZHU, FENG-YI HUANG, XIAO-MING XIONG, and SHI-XUN ZHOU, Phys. Rev. B **37**, 8992 (1988).
[19] YUN ZHU and SHI-XUN ZHOU, J. Phys. A **21**, 1361 (1988).
[20] YUN ZHU, HAO CHEN, and SHI-XUN ZHOU, Phys. Rev. B **38**, 4283 (1988).
[21] H. L. CUI, X. J. LU, N. J. M. HORING, and X. L. LEI, Phys. Rev. B **40**, 3443 (1989).
[22] F. Y. HUANG, Phys. Rev. B **41**, 12957 (1990).
[23] F. Y. HUANG, J. Phys. C **2**, 5327 (1990).
[24] A. GOLD and A. GHAZALI, Phys. Rev. B **41**, 7626 (1990).
[25] G. Y. HU and R. F. O'CONNELL, Phys. Rev. B **42**, 1290 (1990).
[26] Q. P. LI and S. DAS SARMA, Phys. Rev. B **41**, 10268 (1990).
[27] Q. P. LI and S. DAS SARMA, Phys. Rev. B **43**, 11768 (1991).
[28] W. QUE, Phys. Rev. B **43**, 7127 (1991).
[29] L. WENDLER, R. HAUPT, and R. PECHSTEDT, Phys. Rev. B **43**, 14669 (1991).
[30] R. HAUPT, L. WENDLER, and R. PECHSTEDT, Phys. Rev. B **44**, 13635 (1991).
[31] L. WENDLER, R. HAUPT, and R. PECHSTEDT, Surface Sci. **263**, 363 (1992).
[32] L. WENDLER and R. HAUPT, Inst. Phys. Conf. Ser. No. 127, 51 (1992).

[33] G. Y. Hu and R. F. O'Connell, Phys. Rev. B **44**, 3140 (1991).
[34] B. S. Mendoza and W. L. Schaich, Phys. Rev. B **43**, 9275 (1991).
[35] B. S. Mendoza and W. L. Schaich, Phys. Rev. B **43**, 6590 (1991).
[36] Q. P. Li and S. Das Sarma, Phys. Rev. B **44**, 6277 (1991).
[37] S.-R. E. Yang and G. C. Aers, Phys. Rev. B **46**, 12456 (1992).
[38] H. L. Zhao, Y. Zhu, L. Wang, and S. Feng, Phys. Letters A **142**, 36 (1989).
[39] L. Wendler and V. G. Grigoryan, submitted to Phys. Rev. Letters.
[40] G. Gumbs, D. Huang, and D. Heitmann, Phys. Rev. B **44**, 8084 (1991).
[41] L. Wendler and R. Pechstedt, phys. stat. sol. (b) **141**, 129 (1987).
[42] L. Brey, N. F. Johnson, and B. I. Halperin, Phys. Rev. B **40**, 10647 (1989).
[43] L. Wendler, V. G. Grigoryan, and R. Haupt, Superlattices and Microstructures **12**, 501 (1992).
[44] H. Ehrenreich and M. H. Cohen, Phys. Rev. **115**, 786 (1959).
[45] S. Tomonaga, Progr. theor. Phys. **5**, 544 (1950).
[46] J. M. Luttinger, J. math. Phys. (New York) **4**, 1154 (1963).
[47] D. Dahl and L. J. Sham, Phys. Rev. B **16**, 651 (1977).
[48] A. Equiluz and A. A. Maradudin, Ann Phys. (USA) **113**, 29 (1978).
[49] L. Wendler and E. Kändler, phys. stat. sol. (b) **177**, 9 (1993).
[50] L. Wendler and V. G. Grigoryan, submitted to Phys. Rev. B.
[51] A. V. Chaplik and M. V. Krasheninnikov, Surface Sci. **98**, 533 (1980).

(Received June 16, 1993; in revised form October 21, 1993)